ACS NANO

www.acsnano.org

ARTICLE

Apolipoprotein Mimetic Peptide Inhibits Neutrophil-Driven Inflammatory Damage via Membrane Remodeling and Suppression of Cell Lysis

Michelle W. Lee,[¶] Elizabeth Wei-Chia Luo,[¶] Carlos Silvestre-Roig,[¶] Yashes Srinivasan,[¶] Kiyotaka Akabori, Patricia Lemnitzer, Nathan W. Schmidt, Ghee Hwee Lai, Christian D. Santangelo, Oliver Soehnlein,* and Gerard C. L. Wong*

Cite This: *ACS Nano* 2021, 15, 15930–15939

Read Online

ACCESS | Metrics & More | Article Recommendations | Supporting Information

ABSTRACT: **Neutrophils are crucial for host defense but are notorious for causing sterile inflammatory damage. Activated neutrophils in inflamed tissue can liberate histone H4, which was recently shown to perpetuate inflammation by permeating membranes via the generation of negative Gaussian curvature (NGC), leading to lytic cell death. Here, we show that it is possible to build peptides or proteins that cancel NGC in membranes and thereby suppress pore formation, and demonstrate that they can inhibit H4 membrane remodeling and thereby reduce histone H4-driven lytic cell death and resultant inflammation. As a demonstration of principle, we use apolipoprotein A-I (apoA-I) mimetic peptide apoMP$_1$. X-ray structural studies and theoretical calculations show that apoMP$_1$ induces nanoscopic positive Gaussian curvature (PGC), which interacts with the NGC induced by the N-terminus of histone H4 (H4n) to inhibit membrane permeation. Interestingly, we show that induction of PGC can inhibit membrane-permeating activity in general and "turn off" diverse membrane-permeating molecules besides H4n. *In vitro* experiments show an apoMP$_1$ dose-dependent rescue of H4 cytotoxicity. Using a mouse model, we show that tissue accumulation of neutrophils, release of neutrophil extracellular traps (NETs), and extracellular H4 all strongly correlate independently with local tissue cell death in multiple organs, but administration of apoMP$_1$ inhibits histone H4-mediated cytotoxicity and strongly prevents organ tissue damage.**

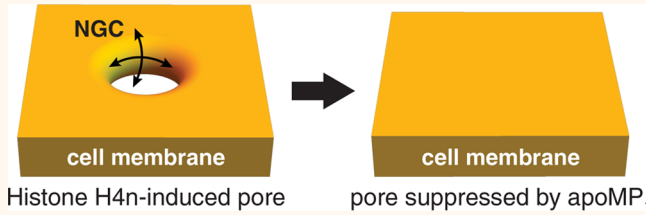

KEYWORDS: *chronic inflammation, neutrophils, apolipoprotein, membrane remodeling, peptide−membrane interactions, cell death*

INTRODUCTION

Although neutrophils play important roles in host defense, they can also precipitate inflammation and tissue damage. Prolonged neutrophil infiltration stimulates inflammation and impedes its resolution.[1] Neutrophil activation triggers the release of inflammatory mediators such as cytokines, granule proteins, and neutrophil extracellular traps (NETs).[2] Excessive accumulation of such mediators promotes the destruction of the host tissue, resulting in nonresolving pathogenic inflammation. This pathogenic role of neutrophils is exemplified by multiple inflammatory pathologies including neurodegenerative diseases, obesity, arthritis, and sepsis.[1] Recent work indicates that proteins bound to NETs are involved in mediating neutrophil-associated damage. NETs are networks of extracellular fibers composed of DNA and externalized proteins of granule, cytoplasmic, and nuclear origin,[3] including histones, the release of which upon cell damage induces tissue damage.[4,5] A machine-learning classifier[6] suggested that the N-terminus of histone H4 (H4n) has the capacity to generate negative Gaussian curvature (NGC) in lipid membranes,[3] a geometric requirement for membrane-permeating processes such as pore formation,[7] which can lead to cell death,[8] itself a potent pro-inflammatory signal. Small-angle X-ray scattering (SAXS) experiments confirmed these predictions.[3] Moreover, in hypercholesterolemic mouse models of atherosclerosis,[9] H4n induced lytic cell death in smooth muscle cells (SMCs),

Received: May 11, 2021
Accepted: September 17, 2021
Published: September 29, 2021

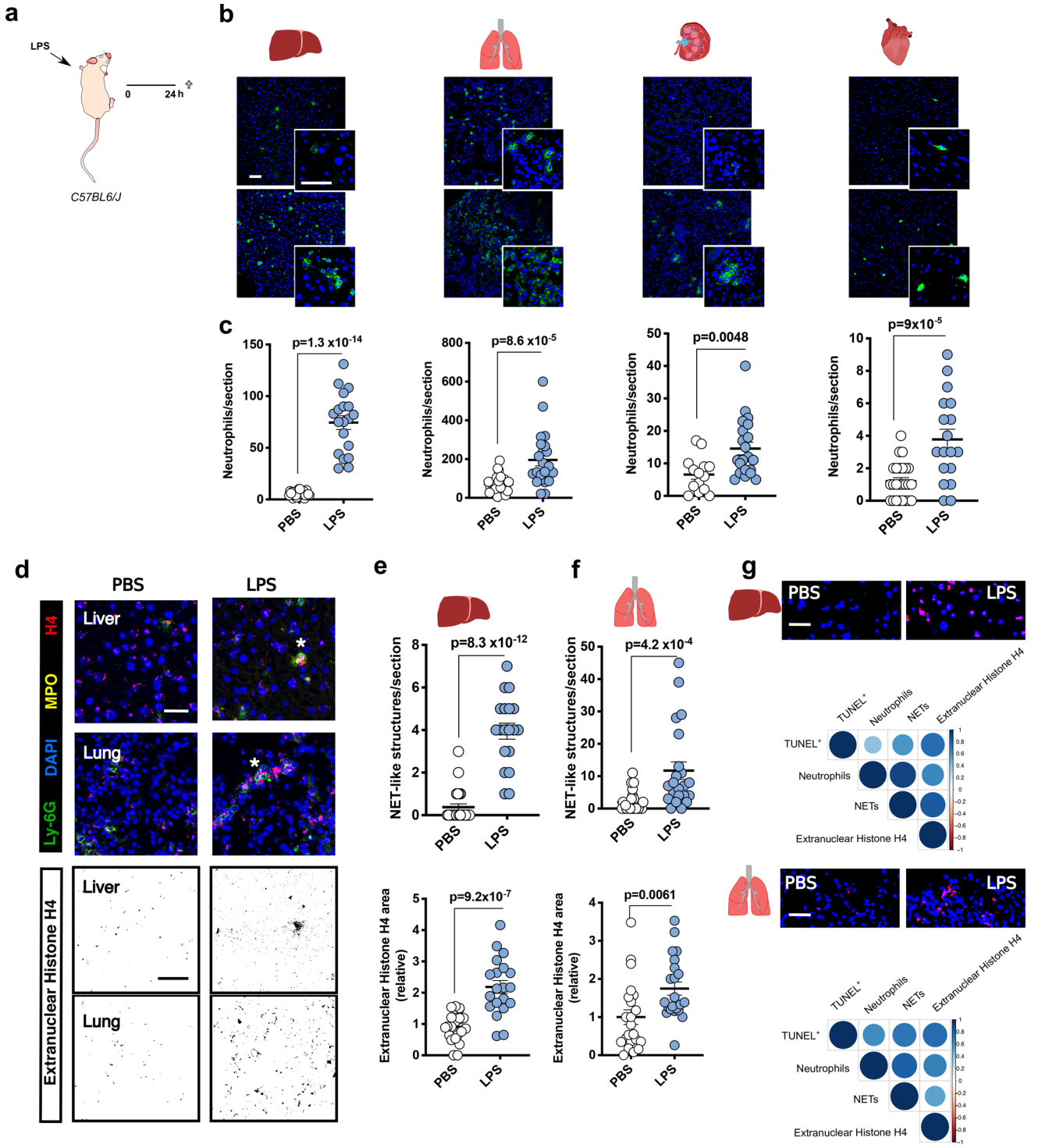

Figure 1. LPS-induced endotoxemia associates with multiorgan neutrophil infiltration, NET release, and tissue damage. (a–g) C57BL/6J mice were challenged with 10 mg/kg of LPS (*E. coli* O111:B4) or vehicle (PBS) for 24 h. (a) Schematic representation of the endotoxemia model. (b, c) From left to right, liver, lung, kidney, and heart. (b) Representative immunofluorescence micrographs showing tissue-infiltrated neutrophils (Ly6G, green) and nuclei (DAPI, blue) in indicated organs. Scale bar: 50 μm. (c) Quantification of infiltrated neutrophils in sections from indicated organs of PBS- or LPS-treated mice. n = 4–5 mice/group. (d) Representative immunofluorescence micrographs showing tissue NET-like structures (indicated with an asterisk) defined with the markers Ly6G, myeloperoxidase (MPO), histone H4, and DNA (DAPI), and extranuclear histone H4 in indicated organs. Extranuclear histone H4 is displayed as a binary image obtained from the subtraction of DAPI signal from histone H4 signal. Scale bar: 50 μm. Quantification of NETs (upper panel) and extranuclear histone H4 area (lower panel) in sections from liver (e) and lung (f) of PBS- or LPS-treated mice. n = 4–5 mice/group. (g) Representative immunofluorescence micrographs showing dead cells (TUNEL, red) and nuclei (DAPI, blue). Scale bar: 50 μm. Correlogram showing Pearson correlations between tissue TUNEL$^+$ cells, neutrophil and NET numbers, and extranuclear histone H4 area in liver (upper panel) and lung (lower panel). n = 9–10 mice. Two-tailed t-test was used unless otherwise stated. All data is represented as mean ± SEM.

https://doi.org/10.1021/acsnano.1c03978
ACS Nano 2021, 15, 15930–15939

also consistent with machine learning and structural studies.[3] Clearly, regaining control of membrane permeation has important immunological consequences in suppressing runaway neutrophil-driven inflammation.

In this work, we show conceptually how peptides or proteins that induce positive Gaussian curvature (PGC, dome-shaped surface curvature) can suppress NGC (saddle-shaped surface curvature) and its consequences, including membrane permeation, lytic cell death, and associated organ damage from inflammation using a combination of synchrotron SAXS measurements, mean-field theory, *in vitro* cell studies, and *in vivo* animal studies. As a demonstration of principle, we use apoMP$_1$, a peptide mimic of apolipoprotein A-I (apoA-I), which is a protein that promotes PGC and organizes lipids into compact spherical high-density lipoprotein (HDL) particles for reverse cholesterol transport. Results from X-ray measurements and theoretical studies show that apoMP$_1$ induces nanoscopic PGC, which interacts with the NGC induced by H4n to inhibit NGC consequences such as membrane permeation. Consistent with this, *in vitro* experiments using murine endothelial cells, SMCs, macrophages, and hepatocytes show an apoMP$_1$ dose-dependent rescue of H4 cytotoxicity. Using a mouse model, we show that tissue accumulation of neutrophils, release of NETs, and extracellular H4 all strongly correlate independently with local tissue cell death in multiple organs, but administration of apoMP$_1$ inhibits histone H4-mediated cytotoxicity and strongly prevents organ tissue damage. These results exemplify a general mechanism for the suppression of membrane permeation that is mediated by membrane curvature rather than allosteric binding. The generality of these membrane-mediated interactions is highlighted with apoMP$_1$'s ability to "turn off" the membrane-remodeling activities of antimicrobial peptides (AMPs) and cell-penetrating peptides (CPPs), which are known to generate NGC in lipid membranes.[7,10−14] To show that these effects are not limited to apolipoprotein-like peptides and to validate this general concept of canceling out induced NGC by applying PGC, we design a peptide and demonstrate that it is also able to suppress the effects of membrane-disruptive peptides. Taken together, these results imply that histone-mediated cell death can be modulated with greater precision and resolution than previous thought possible through controlled membrane remodeling. More notably, the application of curvature as a means to nonspecifically inhibit membrane-remodeling events will help inform the development of therapeutics to treat conditions such as chronic inflammation.

The generation of NGC by pore-forming peptides is well-known.[7,10−12] To study the interaction between induced NGC and PGC in membranes, we need peptide sequences that (1) can generate nanoscopic positive curvature and (2) are soluble and able to freely exchange between different membranes. Lipoproteins are macromolecular complexes that consist of a hydrophobic core of neutral lipids, such as triglycerides and cholesteryl esters, surrounded by an outer layer of phospholipids, free cholesterol, and proteins. Lipoprotein particles are grouped into four major classes based on their density and size: chylomicrons, very low-density lipoproteins (VLDL), low-density lipoproteins (LDL), and HDL. Apolipoproteins, the protein component of lipoproteins, stabilize the geometric structure of lipoprotein particles as they undergo compositional modifications and are broadly classified into two groups, exchangeable (water-soluble) apolipoproteins, which can transfer between lipoprotein particles, and nonexchangeable (water-insoluble) apolipoproteins, which remain bound to the same lipoprotein particle from biosynthesis to breakdown. The transport of lipids is typically facilitated by exchangeable apolipoproteins due to their ability to reversibly associate and dissociate from lipoproteins.[15−18] Exchangeable apolipoproteins are composed of multiple amphipathic α-helices,[19,20] which have been grouped into taxonomies based on their physicochemical properties.[15,21] While the distribution of different classes of amphipathic helices varies both within and among the different apolipoproteins and is believed to account for their diverse lipid affinities and functional properties,[22,23] details of how such helices enforce and maintain distinct lipoprotein structures are not known.

ApoA-I, an exchangeable apolipoprotein that contains 10 amphipathic α-helical segments, is the major protein constituent of HDL particles[24,25] and is central to HDL generation.[26] ApoA-I assembles and stabilizes lipids into spherical HDL species that are 7−12 nm in diameter.[24,27] When mixed, apoA-I and phospholipids are shown to spontaneously associate to form small micelle-like protein−lipid complexes.[15,28,29] Taken together, these findings suggest that the physicochemical properties and characteristics of apoA-I are conducive to the generation of PGC, although it is not clear *a priori* whether the quantitative amount of induced PGC is sufficient to turn off NGC needed for pore formation. Moreover, apoA-I being an exchangeable apolipoprotein allows for its diffusion and recycling between different cell membranes. Peptide analogs have been designed to mimic the lipid-associating helices of apoA-I.[30−34] Despite not having sequence homology to apoA-I, these mimetic peptides have individually been shown to recapitulate different aspects of apoA-I properties,[35−37] including, interestingly, some anti-inflammatory properties.[38] However, given the molecular differences between apoA-I and its peptide analogs and among the peptide analogs, the molecular basis of their therapeutic effects in dampening inflammation is not clear. On the basis of these considerations, we choose a well-characterized apoA-I mimetic peptide (apoMP) DWFKA-FYDKVAEKFKEAF[30,39] (D4F, which we refer to herein as apoMP$_1$ to emphasize its origin and functional role in self-assembly of compact spherical lipid particles).

RESULTS AND DISCUSSION

Uncontrolled inflammatory responses that occur during systemic inflammation can cause tissue destruction, multiorgan failure, and death.[40] Neutrophil hyperactivation in response to bacterial products triggers the release of NETs, the accumulation of which is associated with mortality during septicemia.[4] To interrogate the importance of NET-derived histone H4 on organ tissue damage during systemic inflammation, we administered lipopolysaccharide (LPS) from *E. coli* (O111:B4) intravenously in mice to mimic systemic Gram-negative bacterial infection (Figure 1a). LPS-induced endotoxemia associated with neutrophil activation and triggered multiorgan neutrophil infiltration (Figure 1b,c). In particular, in organs such as the lung and liver, which are especially vulnerable during endotoxemia, LPS infusion induced NET release and the accumulation of extranuclear histone H4 (Figure 1d−f), both of which were positively associated with increased tissue cell death (Figure 1g). Importantly, the levels of extranuclear histone H4 in the tissue positively correlated with the number of infiltrated neutrophils, hence suggesting that tissue histone H4 is of neutrophil origin.

https://doi.org/10.1021/acsnano.1c03978
ACS Nano 2021, 15, 15930−15939

Collectively, systemic activation of circulating neutrophils results in their entrapment in multiple tissues and the release of NET-derived histone H4 to cause tissue damage.

Using a mouse model of endotoxemia, we demonstrated that histone H4 molecules released during NETosis induce tissue damage and cell death in multiple organ systems. In previous studies, we showed that H4n can directly interact with cell membranes, remodel membrane curvature, and promote lytic cell death.[3] H4n consists of 24 amino acids, which include two α-helical segments in the α1 domain of the full histone H4 protein (Figure 2a). Its capacity to form membrane pores has

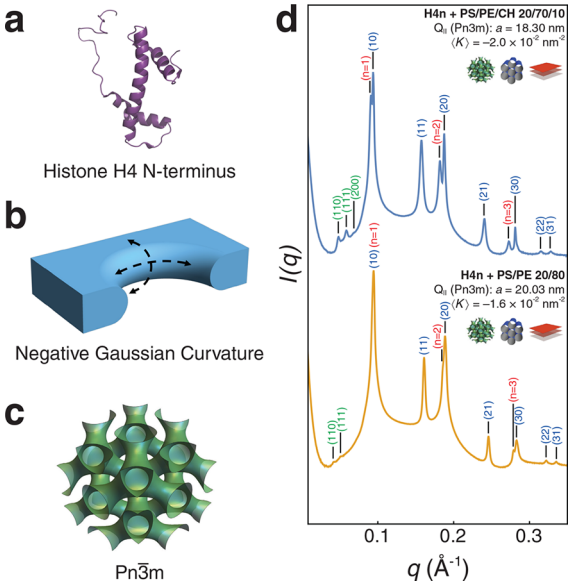

Figure 2. Histone H4 N-terminus induces stronger negative Gaussian curvature in cholesterol-rich membranes. (a) Rendering of H4n. (b) Model of NGC generation by H4n. (c) Representation of the *Pn3m* Q_{II} phase. (d) SAXS spectra of H4n incubated with cholesterol-rich (PS/PE/CH 20/70/10) and cholesterol-poor (PS/PE 20/80) membranes at a P/L molar ratio of 1/40. H4n induces NGC in the form of a *Pn3m* Q_{II} phase. Cholesterol enhances the membrane activity of H4n. Observed reflections for the cubic (green), hexagonal (blue), and lamellar (red) phases have been assigned on the spectra.

been attributed to the ability of its N-terminal domain to induce NGC in cell membranes, which is a geometric requirement for membrane-permeating events. Curvature at a point on a surface can be described by its principal curvatures, c_1 and c_2, along orthogonal axes. For a saddle-shaped deformation, the surface bends in opposite directions along these axes ($c_1 > 0$, $c_2 < 0$), resulting in a Gaussian curvature, $K \equiv c_1c_2$, that is negative (Figure 2b). These saddle-shaped surfaces are required to form the inner surface of a transmembrane pore and the bases of blebs.

Before assessing how $apoMP_1$ may influence the pore-forming activity of H4n, we conducted a control study to confirm H4n's ability to generate membrane-destabilizing curvature at lipid compositions of interest. Small unilamellar vesicles (SUVs) were prepared from ternary lipid mixtures of phosphatidylserine (PS), phosphatidylethanolamine (PE), and cholesterol (CH) at molar ratios of PS/PE 20/80 and PS/PE/CH 20/70/10. Because cholesterol constitutes a large fraction of mammalian cell membranes,[41] we used physiologically relevant cholesterol-containing SUVs to examine the effect of cholesterol on the membrane-remodeling properties of H4n. For the model membrane PS/PE 20/80, we observed a coexistence of three phases: (1) a lamellar phase (L_α) (peaks with q-ratios 1:2:3), (2) an inverse hexagonal phase (H_{II}) (peaks with q-ratios $\sqrt{1}:\sqrt{3}:\sqrt{4}:\sqrt{7}:\sqrt{9}:\sqrt{12}:\sqrt{13}$), and (3) a *Pn3m* inverse bicontinuous cubic phase (Q_{II}) with a lattice parameter of 20.03 nm (peaks with q-ratios $\sqrt{2}:\sqrt{3}:\sqrt{4}$) (Figure 2d). The *Pn3m* phase is rich in NGC (Figure 2c). For the cholesterol-containing model membrane PS/PE/CH 20/70/10, we again observed a similar phase coexistence but with a smaller lattice parameter in the *Pn3m* phase (18.30 nm) (Figure 2d, Table S1). In comparison, the control samples of PS/PE 20/80 SUVs only showed a broad feature of unilamellar vesicles and the control samples of PS/PE/CH 20/70/10 SUVs only exhibited an H_{II} phase (Figure S1). To compare the *Pn3m* phases between cholesterol-rich and cholesterol-poor systems, we calculated the average amount of Gaussian curvature generated in each system using the equation $\langle K \rangle = 2\pi\chi/A_0a^2$, where a is the lattice parameter. The Euler characteristic, χ, and the surface area per unit cell, A_0, are specific for each cubic phase. For *Pn3m*, $\chi = -2$ and $A_0 = 1.919$. An increase in NGC magnitude from $\langle K \rangle = -1.6 \times 10^{-2}$ nm^{-2} for the PS/PE 20/80 membrane to $\langle K \rangle = -2.0 \times 10^{-2}$ nm^{-2} for the PS/PE/CH 20/70/10 membrane indicates that the presence of cholesterol promotes the ability of the H4n to generate membrane curvature. Interestingly, the magnitudes of NGC measured here are comparable with those generated by more hydrophobic AMPs with nonspecific activity against eukaryotic cells,[42] consistent with the contention of lytic cell death, and are within range of previous measurements for H4n.[3] Moreover, SAXS measurements indicate that H4n's ability to generate membrane-permeating curvature and lytic cell death increases with cholesterol content, which typically constitutes 30−40%[41] of mammalian cell membranes.

We hypothesized that apoMPs can interact with membranes in a manner that interferes with the membrane activity of histone H4 and, consequently, attenuate neutrophil-driven cytotoxicity and alleviate associated inflammation. We therefore investigated in detail the effect of $apoMP_1$ on NGC generation by H4n. We incubated PS/PE/CH 20/70/10 SUVs with H4n at a peptide-to-lipid (P/L) molar ratio of 1/40 and $apoMP_1$ at P/L molar ratios of 1/100, 1/50, and 1/25. SAXS measurements had shown that H4n alone induced correlation peaks characteristic of coexisting L_α, H_{II}, and *Pn3m* Q_{II} phases rich in NGC (Figure 2d). When coadministered with $apoMP_1$, however, the NGC-rich *Pn3m* cubic phases generated by H4n gradually disappeared with increasing concentration of $apoMP_1$ (Figure 3a, Table S1). These results imply that $apoMP_1$ can suppress effects associated with NGC generation (Figure 3e).

Interestingly, given that apolipoproteins are not known to bind histones, our results suggest that H4n and $apoMP_1$ interact with one another via a different mechanism rather than direct binding and allosteric inhibition. Since apoA-I assembles spheroidal HDL particles with small radii, it can stabilize positive membrane curvature by definition. Furthermore, deleting the helices that have the highest lipid affinities causes apoA-I to form larger particles, which have less positive curvature.[43] Consistent with that expectation, we find experimentally that $apoMP_1$ can transform an inverse hexagonal phase with strong negative mean curvature into a lamellar phase with zero mean curvature (Figure 3d). To test the idea that an apoMP may suppress H4n pore-forming activity via membrane-mediated interactions, we developed a

https://doi.org/10.1021/acsnano.1c03978
ACS Nano 2021, 15, 15930−15939

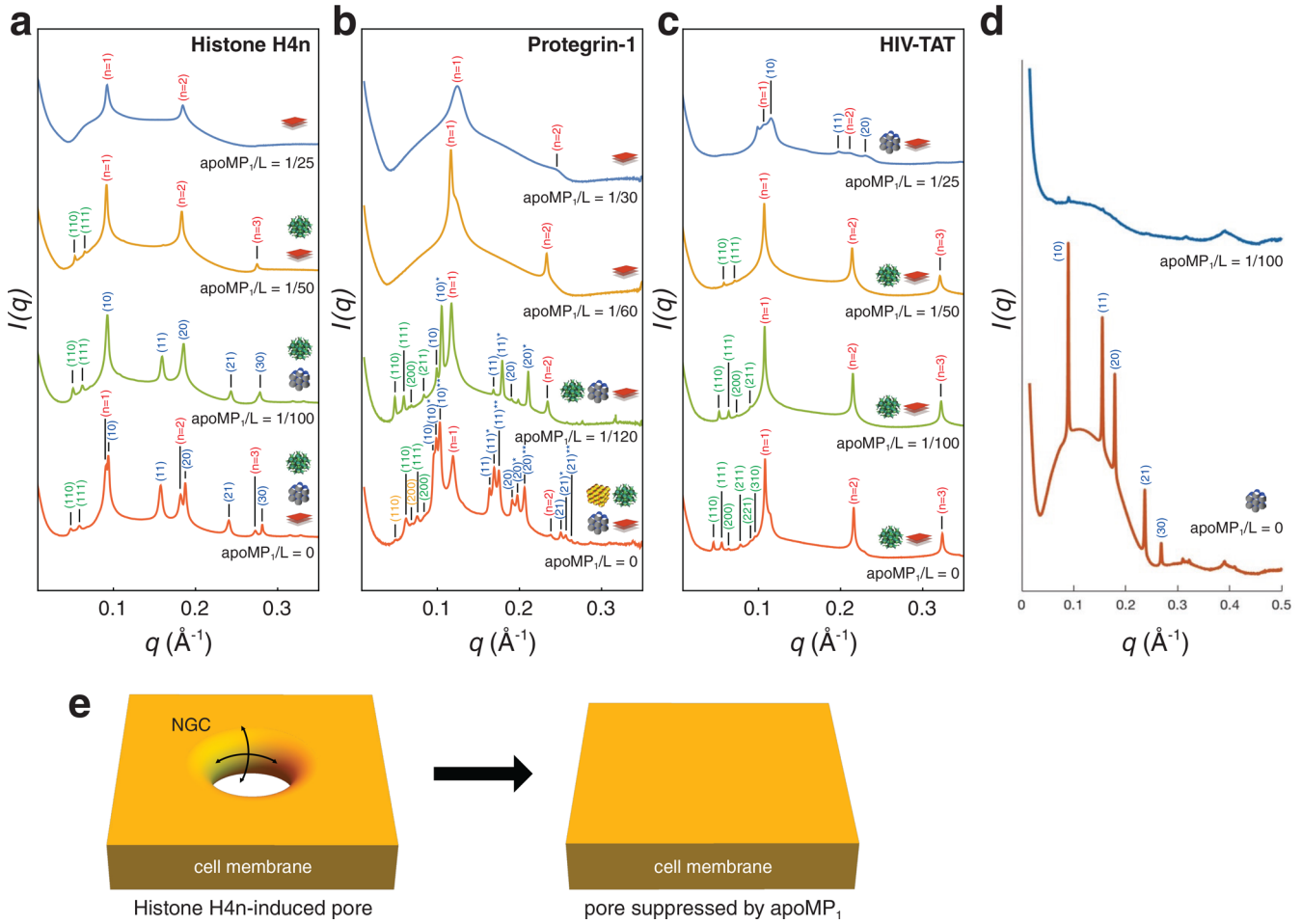

Figure 3. Apolipoprotein A-I mimic apoMP$_1$ inhibits the pro-lytic membrane activity of histone H4 N-terminus and unrelated peptides. (a) SAXS spectra of PS/PE/CH 20/70/10 SUVs incubated with H4n and apoMP$_1$. The P/L molar ratio of H4n was held constant at 1/40, while the P/L molar ratio of apoMP$_1$ was varied. H4n alone induced L_α, H_{II}, and *Pn3m* Q_{II} phases. *Pn3m* Q_{II} phases were suppressed at high concentrations of apoMP$_1$. (b) SAXS spectra of PS/PE 20/80 SUVs cotreated with the AMP PG-1 (NGC-generating peptide) and apoMP$_1$. The P/L molar ratio of PG-1 was held constant at 1/40, while the P/L molar ratio of apoMP$_1$ was varied. PG-1 alone induced L_α, H_{II}, *Pn3m* Q_{II}, and *Im3m* Q_{II} phases. *Pn3m* and *Im3m* Q_{II} phases were suppressed at high P/L molar ratios of apoMP$_1$, leaving behind a zero-curvature L_α phase. (c) SAXS spectra of PS/PE 20/80 SUVs cotreated with the CPP HIV-TAT (NGC-generating peptide) and apoMP$_1$. The P/L molar ratio of HIV-TAT was held constant at 1/40, while the P/L molar ratio of apoMP$_1$ was varied. HIV-TAT alone induced L_α and *Pn3m* Q_{II} phases. *Pn3m* Q_{II} phases were suppressed at high P/L molar ratios of apoMP$_1$, leaving behind L_α and H_{II} phases. (d) ApoMP$_1$ can transform an H_{II} phase with strong negative mean curvature into an L_α phase with zero mean curvature. (a–d) Observed reflections for the *Pn3m* cubic (green), *Im3m* cubic (yellow), hexagonal (blue), and lamellar (red) phases have been assigned on the curves. (e) Schematic portrayal of the suppression of H4n-induced NGC and pore formation by apoMP$_1$.

theoretical model (Supporting Information) for mixtures of two membrane-bound peptides (or proteins), one inducing negative (−) Gaussian curvature (e.g., saddle-shaped deformations from H4n) and the other inducing positive (+) Gaussian curvature (e.g., dome-shaped deformations from apoMP$_1$), in which positive curvature is induced in the membrane with no assumed preferred direction. Each peptide is taken to induce local principal curvatures in the membrane, ξ_1 and ξ_2, which work against the membrane deformations given by the Helfrich free energy over the membrane area $F_{\text{Helfrich}} = (\kappa/2)\int dA(c_1 + c_2)^2$ with bending rigidity κ. The energy of a single ($\pm$) peptide is $E_\pm/(k_B T) = (\lambda/2)[(c_1 - \xi_{1,\pm})^2 + (c_2 - \xi_{2,\pm})^2]$ when the peptide's maximal curvature is aligned with the membrane's, where $(\lambda/2)(\xi_{1,\pm}^2 + \xi_{2,\pm}^2)$ is the energy cost of binding a peptide to a flat membrane, λ is a dimensionless coupling constant, and the induced principal curvatures depend on the peptide type. Analogous to classical nucleation theory, the free energy scales as $E = -\sigma\pi r^2 + 2\pi r\Gamma$ for a pore of radius r and pore rim line tension Γ on a membrane with effective surface tension σ. This model exhibits an energy barrier $E_{\text{barrier}} = \pi\Gamma^2/\sigma$ at a radius $r_0 = \Gamma/\sigma$. When this energy is comparable to thermal energy, pore formation becomes favorable. Mixtures of peptides inducing competing curvatures can control pore formation via this free energy barrier. We find that $K < 0$-inducing peptides, such as H4n, universally suppress the free energy barrier, while peptides that induce PGC ($K > 0$), such as apoMP$_1$, raise the barrier drastically even at modest area fractions (Figure 4a). The precise values used for constants do not change the generic behavior observed in the model. Additionally, the model predicts that the cubic phase lattice parameter a_{Pn3m} generally grows with increasing $K > 0$-inducing to $K < 0$-inducing peptide ratio (Figure 4b). (To see a summary of the interplay between Gaussian curvature, Gaussian modulus $\bar{\kappa}$,

https://doi.org/10.1021/acsnano.1c03978
ACS Nano 2021, 15, 15930−15939

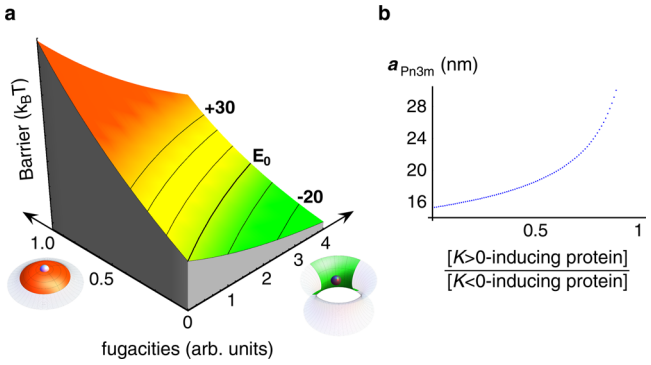

Figure 4. Positive Gaussian curvature induced by peptides can restrain pores formed by negative Gaussian curvature-inducing peptides: (a) Barrier height of pore formation for mixtures of K > 0-inducing (orange) and K < 0-inducing (green) peptides or proteins in theoretical model (Supporting Information). Barrier without proteins E_0 given by $E_0/k_BT = \pi\Gamma_0^2/\sigma_0$, with contours 10 k_BT apart. (b) Protein-prescribed curvatures mapped into corresponding equilibrium a_{Pn3m}, which grow with increasing molar ratio of K > 0-generating to K < 0-generating proteins, consistent with H4n/apoMP$_1$ experimental trends.

and the propensity for pore formation, we refer the interested reader to a recent review.[44])

The suppression mechanism of membrane permeation described by the above theoretical model does not require specific binding between the two types of peptides. To investigate the generality of apoMP$_1$-induced NGC suppression, we examined whether apoMP$_1$ could turn off NGC generated by amphiphilic peptides unrelated to histone-induced inflammation and with no sequence homology to histones, including the AMP protegrin-1 (PG-1) and the CPP human immunodeficiency virus type 1 trans-activator of transcription (HIV-TAT). PG-1 is an 18-amino acid β-hairpin structure[45] and possesses broad-spectrum antimicrobial activity against bacteria, fungi, and viruses[46] via membrane disruption.[47] We incubated PS/PE 20/80 SUVs with PG-1 at a P/L molar ratio of 1/40. PG-1 alone induced correlation peaks characteristic of coexisting L_α, H_{II}, *Pn3m* Q_{II}, and *Im3m* Q_{II} phases (Figure 3b, Table S1). ApoMP$_1$ exhibited dose-dependent suppression of the NGC induced by PG-1: apoMP$_1$ first suppressed the *Im3m* phase at a P/L ratio of 1/120 before completely eliminating NGC, as evidenced by the absence of *Pn3m* phase peaks at a P/L ratio of 1/60. Similarly, apoMP$_1$ suppresses NGC generated by the CPP HIV-TAT,[14] a protein that enhances viral transcription.[48] HIV-TAT alone at a P/L ratio of 1/40 remodeled PS/PE 20/80 SUVs into L_α and *Pn3m* Q_{II} phases. In the presence of apoMP$_1$, at increasing P/L ratios from 1/100 to 1/25, NGC was again suppressed in a dose-dependent manner. At the

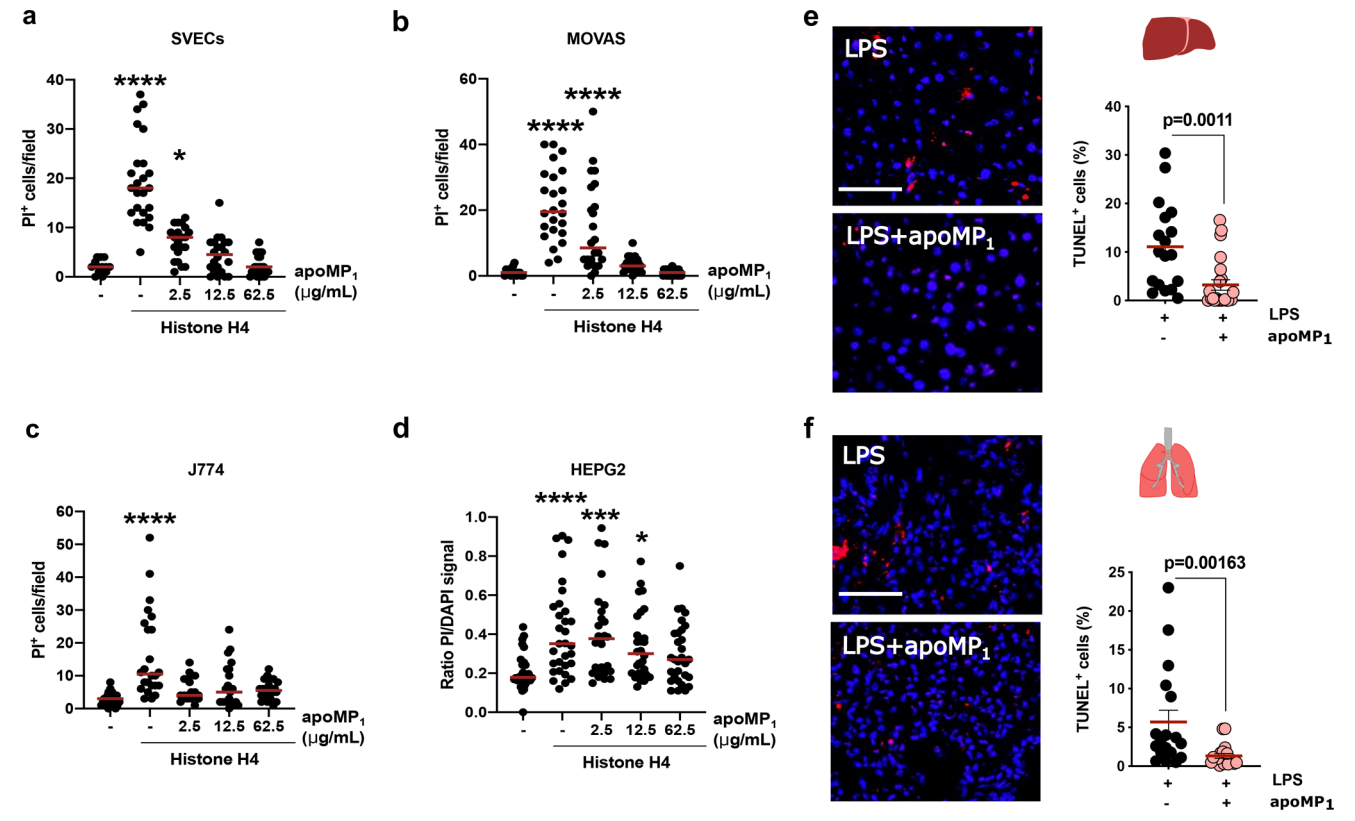

Figure 5. ApoMP$_1$ blocks histone H4-mediated cytotoxicity and prevents organ tissue damage after LPS-induced endotoxemia. (a–d) Histone H4-induced cell death quantified by PI uptake in murine endothelial cells (a), smooth muscle cells (b), macrophages (c), and hepatocytes (d) treated with indicated doses of apoMP$_1$. n = 13–31 fields. Results obtained from three independent experiments. One-way ANOVA with Dunnett's correction. *, p < 0.05; ***, p < 0.001; ****, p < 0.0001. (e, f) C57BL/6J mice were challenged with 10 mg/kg of LPS (*E. coli* O111:B4) for 24 h and treated with apoMP$_1$ (250 μg/intraperitoneal) or vehicle (saline). Representative immunofluorescence micrographs showing TUNEL$^+$ cells and quantification of percentage of TUNEL$^+$ cells in liver (e) and lung (f). Scale bar: 50 μm. n = 5 mice/group. Two-tailed t-test. All data is represented as mean ± SEM.

https://doi.org/10.1021/acsnano.1c03978
ACS Nano 2021, 15, 15930–15939

highest P/L ratio for apoMP$_1$, the system showed a complete absence of NGC-rich cubic phases (Figure 3c, Table S1). Clearly, apoMP$_1$ was able to suppress NGC generation, not just for H4n, but across disparate membrane-remodeling amphiphilic peptides that span AMPs and CPPs, which are drastically different from H4n in sequence, charge, and hydrophobicity. Certainly, it is possible for pore inhibition to involve direct binding between a pore-inhibiting peptide (or protein) and a pore-forming peptide (or protein),[49] based on their individual attributes. However, the results here demonstrating that a single peptide can suppress the effects of multiple pore-forming peptides indicate that direct binding is not required to inhibit the activity of a pore former and thus suggests that a general, nonspecific mechanism exists in parallel. In fact, the generality of these interactions mediated by induced membrane curvature can be seen in extant work on apoMPs: Despite their sequence diversity and lack of sequence homology to apoA-I, a vast number of apoMPs have successfully recapitulated many of the biological functions of apoA-I by mimicking its physicochemical and structural properties. To emphasize this point and the potential to multiplex different functions into these PGC-generating peptide sequences, we designed an antipore peptide APP-2498 that primarily uses arginine residues for its positively charged residues. In contrast, nearly all studied apoMPs exclusively utilize lysine in their positively charged residue positions.[22,31,33,34,39,50−52] We demonstrate that APP-2498 is capable of similar NGC suppression as apoMP$_1$ (Table S2, Figure S2). Indeed, we expect the existence of a general design architecture for antipore peptides.

SAXS measurements indicate that in the presence of apoMP$_1$, the generation of NGC by H4n is greatly attenuated, suggesting that the peptide is able to inhibit membrane-lytic cell death. Consistent with these observations, apoMP$_1$ was able to strongly inhibit the toxic capacity of H4n in different cell types in a dose-dependent fashion (Figure 5a−d). These effects were pronounced in endothelial cells, smooth muscle cells, and macrophages, while minor, yet significant, for hepatocytes. Next, to explore the therapeutic ability of apoMP$_1$ to prevent histone H4-mediated tissue damage, we treated mice with a single dose of apoMP$_1$ together with LPS administration. Notably, apoMP$_1$ treatment fully abrogated liver (Figure 5e) and lung (Figure 5f) tissue damage caused by LPS-induced hyperinflammation. Overall, our results support a host-tissue protective function of apoA-I through the prevention of NGC generation by neutrophil-derived histone H4.

Placing our results in a broader context, existing studies have shown that administration of either HDL or its primary protein component, apoA-I, exhibit anti-inflammatory and protective effects, including the reduction of atherosclerosis,[53] sepsis,[54,55] tumor growth,[56] macrophage activation,[57] and pro-inflammatory cytokine production.[58] However, due to the high dosages of apoA-I needed to achieve these effects, the design of smaller synthetic peptides to recapitulate the activities of apoA-I has recently attracted attention.[59,60] Both animal and human studies have shown that administration of these mimetic peptides leads to similar anti-inflammatory effects, which can treat conditions such as renal[61] and hepatic[62] inflammation, insulin resistance and diabetes,[36] arthritis,[63] asthma,[64] acute vascular inflammation,[31] and atherosclerosis.[30,33,35,65−68] Despite the ability of these mimetic designs to replicate the activities of HDL and apoA-I, the detailed mechanisms of their shared anti-inflammatory activities have been unclear. The findings presented here now suggest that inhibition of NGC generation in membranes by apoA-I and its mimics may explain some their observed anti-inflammatory effects.

CONCLUSIONS

A major challenge in modern medicine is discovering effective therapeutic strategies to inhibit cell death associated with inflammation, which impacts tissue function even after resolution of the acute inflammatory event. We show that LPS-induced sepsis causes neutrophil hyperactivation and release of NETs containing externalized nuclear proteins, including histone H4. Results here indicate that H4n induces rapid, receptor-independent cell death in multiple organs by generating NGC in cell membranes and forming membrane pores, in a manner that is promoted by cholesterol. Importantly, our findings suggest that an apoA-I mimetic peptide has the capacity to suppress histone-induced pore formation and cell death, and thereby prevent systematic tissue damage, through a membrane-mediated mechanism that is independent from direct protein−protein interactions. Our findings here showing that peptides that can suppress NGC have the ability to prevent systemic tissue and organ damage thus carry significant implications for the treatment of a broad range of inflammatory conditions.

METHODS/EXPERIMENTAL SECTION

Complete details of the experimental materials and methods are provided in the Supporting Information.

Peptides. Peptide apoMP$_1$ was a gift from Srinivasa T. Reddy and Alan M. Fogelman. All other peptides were synthesized by LifeTein using solid-phase synthesis or purchased from Anaspec.

SAXS Experiments. Lyophilized phospholipids were purchased from Avanti Polar Lipids and dissolved in chloroform as individual stock solutions. Lipid mixtures were prepared by combining the lipid stock solutions at the desired molar ratios and subsequently evaporated under nitrogen and desiccated overnight. The resulting dry lipid films were resuspended in aqueous buffer solution and incubated overnight at 37 °C. Lipid suspensions were sonicated until clear and extruded through a 0.2 μm pore filter to form SUVs. SUVs were mixed with peptides at specified P/L molar ratios and characterized using SAXS at the Stanford Synchrotron Radiation Lightsource (SSRL) and the Advanced Light Source (ALS).

Animal Experiments. All mouse experiments were carried out according to the European guidelines for the care and use of laboratory animals. Protocols were approved by the Committee on the Ethics of Animal Experiments of the Regierung von Oberbayern. For the mouse endotoxemia model, C57BL/6J mice were challenged with 10 mg/kg LPS from *E. coli* (O111:B4) and treated with 250 μg of apoMP$_1$ intraperitoneally or saline as control. Mice were sacrificed after 24 h, and lung, liver, kidney, and heart tissues were isolated and processed. Immunofluorescence staining was carried out on fixed cryosections and imaged using confocal microscopy.

Cell Viability Assays. Mouse vascular aorta/smooth muscle cells (MOVAS), J774A.1 macrophages, SVEC4-10 endothelial cells, and HepG2 human hepatocytes were incubated with 50 μg/mL histone H4 (Biomol) and specified amounts of apoMP$_1$. Cell viability was determined by propidium iodide (PI) uptake.

Statistics. Statistical analysis was carried out via GraphPad Prism 7 (GraphPad Software). The ROUT outlier function was used to exclude statistical outliers (Q = 1%). Normal distribution of the data was assessed using the D'Agostino-Pearson omnibus test for normality. Normally distributed data was tested by two-tailed unpaired t-test (one variable) or one-way ANOVA with Tukey's or Dunnet's correction (>2 variables). When 2 factors were analyzed, data was analyzed using two-way ANOVA with Tukey's correction. In

https://doi.org/10.1021/acsnano.1c03978
ACS Nano 2021, 15, 15930−15939

all tests a 95% confidence interval was used, with which $p < 0.05$ was considered a significant difference. Correlograms were generated using *R*. All data is represented as mean ± SEM.

ASSOCIATED CONTENT

Supporting Information

The Supporting Information is available free of charge at https://pubs.acs.org/doi/10.1021/acsnano.1c03978.

Full experimental materials and methods; symmetries, lattice parameters, and NGC values of induced cubic phases; SAXS spectra of control samples, SAXS spectra of membranes treated with NGC-generating peptides and APP-2498, schematic of a single peptide interacting with a curved membrane, and schematic of membrane-bound peptides in a model membrane pore (PDF)

AUTHOR INFORMATION

Corresponding Authors

Oliver Soehnlein − *Institute of Experimental Pathology, Center for Molecular Biology of Inflammation (ZMBE), University of Münster, 48149 Münster, Germany; Department of Physiology and Pharmacology (FyFa), Karolinska Institute, 171 77 Stockholm, Sweden; Institute for Cardiovascular Prevention (IPEK), LMU Munich, 80336 Munich, Germany*; Phone: +49 251 83-53064; Email: soehnlein@uni-muenster.de

Gerard C. L. Wong − *Department of Bioengineering, University of California, Los Angeles, California 90095, United States;* orcid.org/0000-0003-0893-6383; Phone: (310) 794-7684; Email: gclwong@seas.ucla.edu

Authors

Michelle W. Lee − *Department of Bioengineering, University of California, Los Angeles, California 90095, United States;* orcid.org/0000-0003-1613-9501

Elizabeth Wei-Chia Luo − *Department of Bioengineering, University of California, Los Angeles, California 90095, United States;* orcid.org/0000-0002-8663-0446

Carlos Silvestre-Roig − *Institute of Experimental Pathology, Center for Molecular Biology of Inflammation (ZMBE), University of Münster, 48149 Münster, Germany; Institute for Cardiovascular Prevention (IPEK), LMU Munich, 80336 Munich, Germany*

Yashes Srinivasan − *Department of Bioengineering, University of California, Los Angeles, California 90095, United States;* orcid.org/0000-0002-5279-9753

Kiyotaka Akabori − *Department of Physics, University of Massachusetts, Amherst, Massachusetts 01003, United States*

Patricia Lemnitzer − *Institute of Experimental Pathology, Center for Molecular Biology of Inflammation (ZMBE), University of Münster, 48149 Münster, Germany*

Nathan W. Schmidt − *Department of Bioengineering, University of California, Los Angeles, California 90095, United States; Ginkgo Bioworks, Boston, Massachusetts 02210, United States*

Ghee Hwee Lai − *Department of Bioengineering, University of California, Los Angeles, California 90095, United States; Singapore Centre for Environmental Life Sciences Engineering (SCELSE), Nanyang Technological University, Singapore 637551*

Christian D. Santangelo − *Department of Physics, University of Massachusetts, Amherst, Massachusetts 01003, United States; Department of Physics, Syracuse University, Syracuse, New York 13244, United States*

Complete contact information is available at: https://pubs.acs.org/10.1021/acsnano.1c03978

Author Contributions

[¶]M.W.L., E.W.C.L., C.S.R., and Y.S. contributed equally to this work. Authorship order among co-first authors was determined alphabetically. M.W.L., E.W.C.L., C.S.R., Y.S., O.S., and G.C.L.W. designed the research. O.S. and G.C.L.W. supervised the research. M.W.L., E.W.C.L., C.S.R., Y.S., O.S., and G.C.L.W. wrote the manuscript. M.W.L., E.W.C.L., and Y.S. conducted synchrotron SAXS experiments and analyzed data. C.S.R. and P.L. conducted mouse experiments, cell culture experiments, immunofluorescence, and analyzed data. K.A. and C.D.S. developed the theoretical model for membrane curvature canceling. N.W.S. and G.H.L. carried out preliminary experiments and analysis. All authors reviewed and approved the final version of the manuscript.

Notes

The authors declare the following competing financial interest(s): A provisional patent application has been filed based on this work.

ACKNOWLEDGMENTS

We thank Srinivasa T. Reddy and Alan M. Fogelman for the generous gift of apoA-I mimetic peptide apoMP$_1$ and for helpful discussions. M.W.L., N.W.S., G.H.L., and G.C.L.W. are supported by the National Science Foundation (DMR 1808459). E.W.C.L., Y.S., and G.C.L.W. are supported by the National Institutes of Health (R01 AI052453). C.S.R. receives funding from the Deutsche Forschungsgemeinschaft (SFB1123 TP A6) and the Else Kröner-Fresenius-Stiftung. C.D.S. is supported by the National Science Foundation (DMR 1822638). O.S. receives funding from the Deutsche Forschungsgemeinschaft (SO876/11-1, SFB914 TP B8, SFB1123 TP A6, TP B5), the Vetenskapsrådet (2017-01762), the Else Kröner-Fresenius-Stiftung, and the Leducq Foundation. We thank the Stanford Synchrotron Radiation Lightsource (SSRL) (Menlo Park, CA, USA) for access to beamline 4-2 and the Advanced Light Source (ALS) (Berkeley, CA, USA) for access to beamline 7.3.3. Use of the SSRL, SLAC National Accelerator Laboratory, is supported by the U.S. Department of Energy, Office of Science, Office of Basic Energy Sciences under contract no. DE-AC02-76SF00515. The SSRL Structural Molecular Biology Program is supported by the U.S. Department of Energy, Office of Biological and Environmental Research, and by the National Institutes of Health, National Institute of General Medical Sciences (P30GM133894). Use of the resources of the ALS, a U.S. Department of Energy Office of Science User Facility, is supported under contract no. DE-AC02-05CH11231.

REFERENCES

(1) Soehnlein, O.; Steffens, S.; Hidalgo, A.; Weber, C. Neutrophils As Protagonists and Targets in Chronic Inflammation. *Nat. Rev. Immunol.* **2017**, *17*, 248−261.

(2) Papayannopoulos, V. Neutrophil Extracellular Traps in Immunity and Disease. *Nat. Rev. Immunol.* **2018**, *18*, 134−147.

(3) Silvestre-Roig, C.; Braster, Q.; Wichapong, K.; Lee, E. Y.; Teulon, J. M.; Berrebeh, N.; Winter, J.; Adrover, J. M.; Santos, G. S.; Froese, A.; Lemnitzer, P.; Ortega-Gómez, A.; Chevre, R.; Marschner, J.; Schumski, A.; Winter, C.; Perez-Olivares, L.; Pan, C.; Paulin, N.;

Schoufour, T.; et al. Externalized Histone H4 Orchestrates Chronic Inflammation by Inducing Lytic Cell Death. *Nature* **2019**, *569*, 236−240.
(4) Xu, J.; Zhang, X.; Pelayo, R.; Monestier, M.; Ammollo, C. T.; Semeraro, F.; Taylor, F. B.; Esmon, N. L.; Lupu, F.; Esmon, C. T. Extracellular Histones Are Major Mediators of Death in Sepsis. *Nat. Med.* **2009**, *15*, 1318−1321.
(5) Saffarzadeh, M.; Juenemann, C.; Queisser, M. A.; Lochnit, G.; Barreto, G.; Galuska, S. P.; Lohmeyer, J.; Preissner, K. T. Neutrophil Extracellular Traps Directly Induce Epithelial and Endothelial Cell Death: A Predominant Role of Histones. *PLoS One* **2012**, *7*, No. e32366.
(6) Lee, E. Y.; Fulan, B. M.; Wong, G. C. L.; Ferguson, A. L. Mapping Membrane Activity in Undiscovered Peptide Sequence Space Using Machine Learning. *Proc. Natl. Acad. Sci. U. S. A.* **2016**, *113*, 13588−13593.
(7) Schmidt, N. W.; Mishra, A.; Lai, G. H.; Davis, M.; Sanders, L. K.; Tran, D.; Garcia, A.; Tai, K. P.; McCray, P. B.; Ouellette, A. J.; Selsted, M. E.; Wong, G. C. L. Criterion for Amino Acid Composition of Defensins and Antimicrobial Peptides Based on Geometry of Membrane Destabilization. *J. Am. Chem. Soc.* **2011**, *133*, 6720−6727.
(8) Dathe, M.; Wieprecht, T. Structural Features of Helical Antimicrobial Peptides: Their Potential to Modulate Activity on Model Membranes and Biological Cells. *Biochim. Biophys. Acta, Biomembr.* **1999**, *1462*, 71−87.
(9) Silvestre-Roig, C.; de Winther, M. P.; Weber, C.; Daemen, M. J.; Lutgens, E.; Soehnlein, O. Atherosclerotic Plaque Destabilization. *Circ. Res.* **2014**, *114*, 214−226.
(10) Hickel, A.; Danner-Pongratz, S.; Amenitsch, H.; Degovics, G.; Rappolt, M.; Lohner, K.; Pabst, G. Influence of Antimicrobial Peptides on the Formation of Nonlamellar Lipid Mesophases. *Biochim. Biophys. Acta, Biomembr.* **2008**, *1778*, 2325−2333.
(11) Prenner, E. J.; Lewis, R. N. A. H.; Neuman, K. C.; Gruner, S. M.; Kondejewski, L. H.; Hodges, R. S.; McElhaney, R. N. Nonlamellar Phases Induced by the Interaction of Gramicidin S with Lipid Bilayers. A Possible Relationship to Membrane-Disrupting Activity. *Biochemistry* **1997**, *36*, 7906−7916.
(12) Keller, S. L.; Gruner, S. M.; Gawrisch, K. Small Concentrations of Alamethicin Induce a Cubic Phase in Bulk Phosphatidylethanolamine Mixtures. *Biochim. Biophys. Acta, Biomembr.* **1996**, *1278*, 241−246.
(13) Schmidt, N.; Mishra, A.; Lai, G. H.; Wong, G. C. L. Arginine-Rich Cell-Penetrating Peptides. *FEBS Lett.* **2010**, *584*, 1806−1813.
(14) Mishra, A.; Lai, G. H.; Schmidt, N. W.; Sun, V. Z.; Rodriguez, A. R.; Tong, R.; Tang, L.; Cheng, J.; Deming, T. J.; Kamei, D. T.; Wong, G. C. L. Translocation of HIV TAT Peptide and Analogues Induced by Multiplexed Membrane and Cytoskeletal Interactions. *Proc. Natl. Acad. Sci. U. S. A.* **2011**, *108*, 16883−16888.
(15) Segrest, J. P.; Jones, M. K.; De Loof, H.; Brouillette, C. G.; Venkatachalapathi, Y. V.; Anantharamaiah, G. M. The Amphipathic Helix in the Exchangeable Apolipoproteins: A Review of Secondary Structure and Function. *J. Lipid Res.* **1992**, *33*, 141−166.
(16) Remaley, A. T.; Schumacher, U. K.; Stonik, J. A.; Farsi, B. D.; Nazih, H.; Brewer, H. B. Decreased Reverse Cholesterol Transport from Tangier Disease Fibroblasts. *Arterioscler., Thromb., Vasc. Biol.* **1997**, *17*, 1813−1821.
(17) Remaley, A. T.; Stonik, J. A.; Demosky, S. J.; Neufeld, E. B.; Bocharov, A. V.; Vishnyakova, T. G.; Eggerman, T. L.; Patterson, A. P.; Duverger, N. J.; Santamarina-Fojo, S.; Brewer, H. B. Apolipoprotein Specificity for Lipid Efflux by the Human ABCAI Transporter. *Biochem. Biophys. Res. Commun.* **2001**, *280*, 818−823.
(18) Smith, L. E.; Segrest, J. P.; Davidson, W. S. Helical Domains That Mediate Lipid Solubilization and ABCA1-Specific Cholesterol Efflux in Apolipoproteins C-I and A-II. *J. Lipid Res.* **2013**, *54*, 1939−1948.
(19) McLachlan, A. D. Repeated Helical Pattern in Apolipoprotein-A-I. *Nature* **1977**, *267*, 465−466.
(20) Li, W. H.; Tanimura, M.; Luo, C. C.; Datta, S.; Chan, L. The Apolipoprotein Multigene Family: Biosynthesis, Structure, Structure−Function Relationships, and Evolution. *J. Lipid Res.* **1988**, *29*, 245−271.
(21) Segrest, J. P.; De Loof, H.; Dohlman, J. G.; Brouillette, C. G.; Anantharamaiah, G. M. Amphipathic Helix Motif: Classes and Properties. *Proteins: Struct., Funct., Genet.* **1990**, *8*, 103−117.
(22) Mishra, V. K.; Palgunachari, M. N. Interaction of Model Class A1, Class A2, and Class Y Amphipathic Helical Peptides with Membranes. *Biochemistry* **1996**, *35*, 11210−11220.
(23) Saito, H.; Lund-Katz, S.; Phillips, M. C. Contributions of Domain Structure and Lipid Interaction to the Functionality of Exchangeable Human Apolipoproteins. *Prog. Lipid Res.* **2004**, *43*, 350−380.
(24) Davidson, W. S.; Thompson, T. B. The Structure of Apolipoprotein A-I in High Density Lipoproteins. *J. Biol. Chem.* **2007**, *282*, 22249−22253.
(25) Kontush, A.; Chapman, M. J. *High-Density Lipoproteins: Structure, Metabolism, Function, and Therapeutics*; John Wiley & Sons, Inc.: Hoboken, NJ, 2011; p 648.
(26) Mishra, V. K.; Palgunachari, M. N.; Datta, G.; Phillips, M. C.; Lund-Katz, S.; Adeyeye, S. O.; Segrest, J. P.; Anantharamaiah, G. M. Studies of Synthetic Peptides of Human Apolipoprotein A-I Containing Tandem Amphipathic α-Helixes. *Biochemistry* **1998**, *37*, 10313−10324.
(27) Silva, R. A. G. D.; Huang, R.; Morris, J.; Fang, J.; Gracheva, E. O.; Ren, G.; Kontush, A.; Jerome, W. G.; Rye, K.-A.; Davidson, W. S. Structure of Apolipoprotein A-I in Spherical High Density Lipoproteins of Different Sizes. *Proc. Natl. Acad. Sci. U. S. A.* **2008**, *105*, 12176−12181.
(28) Tall, A. R.; Small, D. M.; Shipley, G. G.; Lees, R. S. Apoprotein Stability and Lipid−Protein Interactions in Human Plasma High Density Lipoproteins. *Proc. Natl. Acad. Sci. U. S. A.* **1975**, *72*, 4940−4942.
(29) Atkinson, D.; Smith, H. M.; Dickson, J.; Austin, J. P. Interaction of Apoprotein from Porcine High-Density Lipoprotein with Dimyristoyl Lecithin. *Eur. J. Biochem.* **1976**, *64*, 541−547.
(30) Navab, M.; Anantharamaiah, G. M.; Reddy, S. T.; Hama, S.; Hough, G.; Grijalva, V. R.; Yu, N.; Ansell, B. J.; Datta, G.; Garber, D. W.; Fogelman, A. M. Apolipoprotein A-I Mimetic Peptides. *Arterioscler., Thromb., Vasc. Biol.* **2005**, *25*, 1325−1331.
(31) Di Bartolo, B. A.; Nicholls, S. J.; Bao, S.; Rye, K.-A.; Heather, A. K.; Barter, P. J.; Bursill, C. The Apolipoprotein A-I Mimetic Peptide ETC-642 Exhibits Anti-Inflammatory Properties That Are Comparable to High Density Lipoproteins. *Atherosclerosis* **2011**, *217*, 395−400.
(32) Wool, G. D.; Reardon, C. A.; Getz, G. S. Apolipoprotein A-I Mimetic Peptide Helix Number and Helix Linker Influence Potentially Anti-Atherogenic Properties. *J. Lipid Res.* **2008**, *49*, 1268−1283.
(33) D'Souza, W.; Stonik, J. A.; Murphy, A.; Demosky, S. J.; Sethi, A. A.; Moore, X. L.; Chin-Dusting, J.; Remaley, A. T.; Sviridov, D. Structure/Function Relationships of Apolipoprotein A-I Mimetic Peptides. *Circ. Res.* **2010**, *107*, 217−227.
(34) Mendez, A. J.; Anantharamaiah, G. M.; Segrest, J. P.; Oram, J. F. Synthetic Amphipathic Helical Peptides That Mimic Apolipoprotein A-I in Clearing Cellular Cholesterol. *J. Clin. Invest.* **1994**, *94*, 1698−1705.
(35) Garber, D. W.; Datta, G.; Chaddha, M.; Palgunachari, M. N.; Hama, S. Y.; Navab, M.; Fogelman, A. M.; Segrest, J. P.; Anantharamaiah, G. M. A New Synthetic Class A Amphipathic Peptide Analogue Protects Mice from Diet-Induced Atherosclerosis. *J. Lipid Res.* **2001**, *42*, 545−552.
(36) Morgantini, C.; Imaizumi, S.; Grijalva, V.; Navab, M.; Fogelman, A. M.; Reddy, S. T. Apolipoprotein A-I Mimetic Peptides Prevent Atherosclerosis Development and Reduce Plaque Inflammation in a Murine Model of Diabetes. *Diabetes* **2010**, *59*, 3223−3228.
(37) Van Lenten, B. J.; Wagner, A. C.; Anantharamaiah, G. M.; Navab, M.; Reddy, S. T.; Buga, G. M.; Fogelman, A. M. Apolipoprotein A-I Mimetic Peptides. *Curr. Atheroscler. Rep.* **2009**, *11*, 52−57.

https://doi.org/10.1021/acsnano.1c03978
ACS Nano 2021, 15, 15930−15939

(38) Anantharamaiah, G. M.; Mishra, V. K.; Garber, D. W.; Datta, G.; Handattu, S. P.; Palgunachari, M. N.; Chaddha, M.; Navab, M.; Reddy, S. T.; Segrest, J. P.; Fogelman, A. M. Structural Requirements for Antioxidative and Anti-Inflammatory Properties of Apolipoprotein A-I Mimetic Peptides. *J. Lipid Res.* **2007**, *48*, 1915−1923.
(39) Datta, G.; Chaddha, M.; Hama, S.; Navab, M.; Fogelman, A. M.; Garber, D. W.; Mishra, V. K.; Epand, R. M.; Epand, R. F.; Lund-Katz, S.; Phillips, M. C.; Segrest, J. P.; Anantharamaiah, G. M. Effects of Increasing Hydrophobicity on the Physical-Chemical and Biological Properties of a Class A Amphipathic Helical Peptide. *J. Lipid Res.* **2001**, *42*, 1096−1104.
(40) Angus, D. C.; van der Poll, T. Severe Sepsis and Septic Shock. *N. Engl. J. Med.* **2013**, *369*, 840−851.
(41) Pinkwart, K.; Schneider, F.; Lukoseviciute, M.; Sauka-Spengler, T.; Lyman, E.; Eggeling, C.; Sezgin, E. Nanoscale Dynamics of Cholesterol in the Cell Membrane. *J. Biol. Chem.* **2019**, *294*, 12599−12609.
(42) Lee, M. W.; de Anda, J.; Kroll, C.; Bieniossek, C.; Bradley, K.; Amrein, K. E.; Wong, G. C. L. How Do Cyclic Antibiotics with Activity against Gram-Negative Bacteria Permeate Membranes? A Machine Learning Informed Experimental Study. *Biochim. Biophys. Acta, Biomembr.* **2020**, *1862*, 183302.
(43) Vedhachalam, C.; Chetty, P. S.; Nickel, M.; Dhanasekaran, P.; Lund-Katz, S.; Rothblat, G. H.; Phillips, M. C. Influence of Apolipoprotein (Apo) A-I Structure on Nascent High Density Lipoprotein (HDL) Particle Size Distribution. *J. Biol. Chem.* **2010**, *285*, 31965−31973.
(44) Schmidt, N. W.; Wong, G. C. L. Antimicrobial Peptides and Induced Membrane Curvature: Geometry, Coordination Chemistry, and Molecular Engineering. *Curr. Opin. Solid State Mater. Sci.* **2013**, *17*, 151−163.
(45) Steinberg, D. A.; Hurst, M. A.; Fujii, C. A.; Kung, A. H.; Ho, J. F.; Cheng, F. C.; Loury, D. J.; Fiddes, J. C. Protegrin-1: A Broad-Spectrum, Rapidly Microbicidal Peptide with *in Vivo* Activity. *Antimicrob. Agents Chemother.* **1997**, *41*, 1738−1742.
(46) Kokryakov, V. N.; Harwig, S. S. L.; Panyutich, E. A.; Shevchenko, A. A.; Aleshina, G. M.; Shamova, O. V.; Korneva, H. A.; Lehrer, R. I. Protegrins: Leukocyte Antimicrobial Peptides That Combine Features of Corticostatic Defensins and Tachyplesins. *FEBS Lett.* **1993**, *327*, 231−236.
(47) Lam, K. L. H.; Ishitsuka, Y.; Cheng, Y.; Chien, K.; Waring, A. J.; Lehrer, R. I.; Lee, K. Y. C. Mechanism of Supported Membrane Disruption by Antimicrobial Peptide Protegrin-1. *J. Phys. Chem. B* **2006**, *110*, 21282−21286.
(48) Debaisieux, S.; Rayne, F.; Yezid, H.; Beaumelle, B. The Ins and Outs of HIV-1 TAT. *Traffic* **2012**, *13*, 355−363.
(49) Wang, Y.; Agerberth, B.; Löthgren, A.; Almstedt, A.; Johansson, J. Apolipoprotein A-I Binds and Inhibits the Human Antibacterial/Cytotoxic Peptide LL-37. *J. Biol. Chem.* **1998**, *273*, 33115−33118.
(50) Sethi, A. A.; Stonik, J. A.; Thomas, F.; Demosky, S. J.; Amar, M.; Neufeld, E.; Brewer, H. B.; Davidson, W. S.; D'Souza, W.; Sviridov, D.; Remaley, A. T. Asymmetry in the Lipid Affinity of Bihelical Amphipathic Peptides: A Structural Determinant for the Specificity of ABCA1-Dependent Cholesterol Efflux by Peptides. *J. Biol. Chem.* **2008**, *283*, 32273−32282.
(51) Tanaka, M.; Takamura, Y.; Kawakami, T.; Aimoto, S.; Saito, H.; Mukai, T. Effect of Amino Acid Distribution of Amphipathic Helical Peptide Derived from Human Apolipoprotein A-I on Membrane Curvature Sensing. *FEBS Lett.* **2013**, *587*, 510−515.
(52) Segrest, J. P.; Chung, B. H.; Brouillette, C. G.; Kanellis, P.; McGahan, R. Studies of Synthetic Peptide Analogs of the Amphipathic Helix. Competitive Displacement of Exchangeable Apolipoproteins from Native Lipoproteins. *J. Biol. Chem.* **1983**, *258*, 2290−2295.
(53) Kingwell, B. A.; Chapman, M. J. Future of High-Density Lipoprotein Infusion Therapies. *Circulation* **2013**, *128*, 1112−1121.
(54) Murch, O.; Collin, M.; Hinds, C. J.; Thiemermann, C. Lipoproteins in Inflammation and Sepsis. I. Basic Science. *Intensive Care Med.* **2007**, *33*, 13−24.
(55) Jiao, Y.-l.; Wu, M.-P. Apolipoprotein A-I Diminishes Acute Lung Injury and Sepsis in Mice Induced by Lipoteichoic Acid. *Cytokine+* **2008**, *43*, 83−87.
(56) Zamanian-Daryoush, M.; Lindner, D.; Tallant, T. C.; Wang, Z.; Buffa, J.; Klipfell, E.; Parker, Y.; Hatala, D.; Parsons-Wingerter, P.; Rayman, P.; Yusufishaq, M. S. S.; Fisher, E. A.; Smith, J. D.; Finke, J.; DiDonato, J. A.; Hazen, S. L. The Cardioprotective Protein Apolipoprotein A1 Promotes Potent Anti-Tumorigenic Effects. *J. Biol. Chem.* **2013**, *288*, 21237−21252.
(57) De Nardo, D.; Labzin, L. I.; Kono, H.; Seki, R.; Schmidt, S. V.; Beyer, M.; Xu, D.; Zimmer, S.; Lahrmann, C.; Schildberg, F. A.; Vogelhuber, J.; Kraut, M.; Ulas, T.; Kerksiek, A.; Krebs, W.; Bode, N.; Grebe, A.; Fitzgerald, M. L.; Hernandez, N. J.; Williams, B. R. G.; et al. High-Density Lipoprotein Mediates Anti-Inflammatory Reprogramming of Macrophages *via* the Transcriptional Regulator ATF3. *Nat. Immunol.* **2014**, *15*, 152−160.
(58) Catapano, A. L.; Pirillo, A.; Bonacina, F.; Norata, G. D. HDL in Innate and Adaptive Immunity. *Cardiovasc. Res.* **2014**, *103*, 372−383.
(59) White, C. R.; Garber, D. W.; Anantharamaiah, G. M. Anti-Inflammatory and Cholesterol-Reducing Properties of Apolipoprotein Mimetics: A Review. *J. Lipid Res.* **2014**, *55*, 2007−2021.
(60) Remaley, A. T.; Amar, M.; Sviridov, D. HDL-Replacement Therapy: Mechanism of Action, Types of Agents and Potential Clinical Indications. *Expert Rev. Cardiovasc. Ther.* **2008**, *6*, 1203−1215.
(61) Buga, G. M.; Frank, J. S.; Mottino, G. A.; Hakhamian, A.; Narasimha, A.; Watson, A. D.; Yekta, B.; Navab, M.; Reddy, S. T.; Anantharamaiah, G. M.; Fogelman, A. M. D-4F Reduces EO6 Immunoreactivity, SREBP-1c mRNA Levels, and Renal Inflammation in LDL Receptor-Null Mice Fed a Western Diet. *J. Lipid Res.* **2008**, *49*, 192−205.
(62) McGrath, K. C.; Li, X.; Twigg, S. M.; Heather, A. K. Apolipoprotein-AI Mimetic Peptides D-4F and L-5F Decrease Hepatic Inflammation and Increase Insulin Sensitivity in C57BL/6 Mice. *PLoS One* **2020**, *15*, No. e0226931.
(63) Charles-Schoeman, C.; Banquerigo, M. L.; Hama, S.; Navab, M.; Park, G. S.; Van Lenten, B. J.; Wagner, A. C.; Fogelman, A. M.; Brahn, E. Treatment with an Apolipoprotein A-1 Mimetic Peptide in Combination with Pravastatin Inhibits Collagen-Induced Arthritis. *Clin. Immunol.* **2008**, *127*, 234−244.
(64) Yao, X.; Dai, C.; Fredriksson, K.; Dagur, P. K.; McCoy, J. P.; Qu, X.; Yu, Z.-X.; Keeran, K. J.; Zywicke, G. J.; Amar, M. J. A.; Remaley, A. T.; Levine, S. J. 5A, an Apolipoprotein A-I Mimetic Peptide, Attenuates the Induction of House Dust Mite-Induced Asthma. *J. Immunol.* **2011**, *186*, 576−583.
(65) Ditiatkovski, M.; Palsson, J.; Chin-Dusting, J.; Remaley, A. T.; Sviridov, D. Apolipoprotein A-I Mimetic Peptides. *Arterioscler., Thromb., Vasc. Biol.* **2017**, *37*, 1301−1306.
(66) Zhao, Y.; Imura, T.; Leman, L. J.; Curtiss, L. K.; Maryanoff, B. E.; Ghadiri, M. R. Mimicry of High-Density Lipoprotein: Functional Peptide−Lipid Nanoparticles Based on Multivalent Peptide Constructs. *J. Am. Chem. Soc.* **2013**, *135*, 13414−13424.
(67) Getz, G. S.; Wool, G. D.; Reardon, C. A. HDL Apolipoprotein-Related Peptides in the Treatment of Atherosclerosis and Other Inflammatory Disorders. *Curr. Pharm. Des.* **2010**, *16*, 3173−3184.
(68) Bloedon, L. T.; Dunbar, R.; Duffy, D.; Pinell-Salles, P.; Norris, R.; DeGroot, B. J.; Movva, R.; Navab, M.; Fogelman, A. M.; Rader, D. J. Safety, Pharmacokinetics, and Pharmacodynamics of Oral ApoA-I Mimetic Peptide D-4F in High-Risk Cardiovascular Patients. *J. Lipid Res.* **2008**, *49*, 1344−1352.

https://doi.org/10.1021/acsnano.1c03978
ACS Nano 2021, 15, 15930−15939

Supporting Information For

Apolipoprotein Mimetic Peptide Inhibits Neutrophil-Driven Inflammatory Damage via Membrane Remodeling and Suppression of Cell Lysis

Michelle W. Lee[#1], Elizabeth Wei-Chia Luo[#1], Carlos Silvestre-Roig[#2,3], Yashes Srinivasan[#1], Kiyotaka Akabori[4], Patricia Lemnitzer[2], Nathan W. Schmidt[1,5], Ghee Hwee Lai[1,6], Christian D. Santangelo[4,7], Oliver Soehnlein[2,3,8], Gerard C. L. Wong*[1]*

[1]Department of Bioengineering, University of California, Los Angeles, Los Angeles, CA 90095, United States

[2]Institute of Experimental Pathology, Center for Molecular Biology of Inflammation (ZMBE), University of Münster, 48149 Münster, Germany

[3]Institute for Cardiovascular Prevention (IPEK), LMU Munich, 80336 Munich, Germany

[4]Department of Physics, University of Massachusetts, Amherst, MA 01003, United States

[5]Ginkgo Bioworks, 27 Drydock Avenue, Boston, MA 02210, United States

[6]Singapore Centre for Environmental Life Sciences Engineering (SCELSE), Nanyang Technological University, 60 Nanyang Drive, SBS-01N-27, Singapore 637551

[7]Department of Physics, Syracuse University, Syracuse, NY 13244, United States

[8]Department of Physiology and Pharmacology (FyFa), Karolinska Institute, 171 77 Stockholm, Sweden

[#]Authors contributed equally

*To whom correspondence should be addressed:

Oliver Soehnlein, Email: soehnlein@uni-muenster.de

Gerard C. L. Wong, Email: gclwong@seas.ucla.edu

Materials and Methods

Peptides

Lyophilized histone H4 N-terminus (H4n, S-G-R-G-K-G-G-K-G-L-G-K-G-G-A-K-R-H-R-K-V-L-R-D) and anti-pore peptide APP-2498 (G-D-A-V-R-E-W-F-E-K-A-W-Q-R-V-R-E-F-F) synthesized using solid-phase synthesis were purchased at high purity (>95% HPLC) from LifeTein. Lyophilized protegrin-1 (PG-1, R-G-G-R-L-C-Y-C-R-R-R-F-C-V-C-V-G-R), human immunodeficiency virus type 1 trans-activator of transcription (HIV-TAT, G-R-K-K-R-R-Q-R-R-R-P-Q), and melittin (G-I-G-A-V-L-K-V-L-T-T-G-L-P-A-L-I-S-W-I-K-R-K-R-Q-Q) were purchased from Anaspec. Lyophilized apoA-I mimetic peptide apoMP$_1$ (D-W-F-K-A-F-Y-D-K-V-A-E-K-F-K-E-A-F) was a generous gift from Srinivasa T. Reddy and Alan M. Fogelman.

Preparation of SUVs

Lyophilized phospholipids 1,2-dioleoyl-*sn*-glycero-3-phospho-L-serine (DOPS), 1,2-dioleoyl-*sn*-glycero-3-phosphoethanolamine (DOPE), and cholesterol (CH) purchased from Avanti Polar Lipids were dissolved in chloroform at 20 mg/mL to produce individual stock solutions. Ternary lipid compositions were prepared from these stock solutions as mixtures of DOPS/DOPE/CH at molar ratios of 20/80/0 and 20/70/10, evaporated under nitrogen, and desiccated overnight under vacuum to form dry lipid films. Lipid films were resuspended in physiological aqueous buffer (140 mM NaCl, 10 mM N-(2-hydroxyethyl)piperazine-N'-ethanesulfonic acid (HEPES), pH 7.4) to a concentration of 20 mg/mL. Lipid suspensions were incubated overnight at 37 °C, sonicated until clear, and extruded through a 0.2 μm pore Anotop syringe filter (Whatman) to yield SUVs.

SAXS experiments

Before use, peptides were dissolved in nuclease-free water. Depending on the assay, SUVs were then mixed with peptides at specific P/L molar ratios. Precipitated peptide–lipid complexes were transferred into 1.5 mm quartz capillaries (Hilgenberg GmbH, Mark-tubes) and hermetically sealed with an oxygen torch. SAXS measurements were taken at the Stanford Synchrotron

Radiation Lightsource (SSRL) (beamline 4-2) and the Advanced Light Source (ALS) (beamline 7.3.3) using monochromatic X-rays with energies of 9 keV and 10 keV, respectively. Samples were incubated at 37 °C and centrifuged before measurement. Scattered radiation was collected using DECTRIS PILATUS3 X 1M and PILATUS 2M detectors (both with a 172 μm pixel size) at SSRL and ALS, respectively. The 2D powder diffraction patterns were azimuthally integrated into 1D patterns using the Nika[1] 1.76 package for Igor Pro 7.04 (Wavemetrics). For all samples, multiple measurements were taken at different times to ensure consistency.

To determine the phases present in each sample, the integrated scattering intensity $I(q)$ *versus* q was plotted using Mathematica (Wolfram Research) or MATLAB (MathWorks). The measured q-values corresponding to peak positions were obtained and their ratios were compared to the permitted reflections for different liquid-crystalline lipid phases (e.g., lamellar, hexagonal, cubic). Lamellar phases exhibit integer ratios of 1:2:3 and hexagonal phases exhibit ratios of $\sqrt{1}:\sqrt{3}:\sqrt{4}:\sqrt{7}:\sqrt{9}:\sqrt{12}:\sqrt{13}$. Cubic phases observed in our experiments belonged to the *Pn*3*m* space group, which permits reflections at ratios of $\sqrt{2}:\sqrt{3}:\sqrt{4}:\sqrt{6}:\sqrt{8}:\sqrt{9}$, and the *Im3m* space group, which permits reflections at ratios of $\sqrt{2}:\sqrt{4}:\sqrt{6}:\sqrt{8}:\sqrt{10}:\sqrt{12}:\sqrt{14}:\sqrt{16}$. For each cubic phase, the measured peak positions were related to the Miller indices (h, k, l) of their observed reflections with the equation $q = 2\pi\sqrt{(h^2+k^2+l^2)}/a$, where a is the lattice parameter. The slope of the linear regression for measured q-values *versus* $\sqrt{(h^2+k^2+l^2)}$ was then used to calculate a. The average Gaussian curvature $\langle \boldsymbol{K} \rangle$ per unit cell volume for a cubic phase was calculated using the equation $\langle \boldsymbol{K} \rangle = 2\pi\chi/A_0a^2$, where χ is the Euler characteristic and A_0 is the surface area per cubic unit cell. For *Pn*3*m* cubic phases, $\chi = -2$ and $A_0 = 1.919$. For *Im3m* cubic phases, $\chi = -4$ and $A_0 = 2.345$.

Schematics of cubic phases

The cubic phase representation (Figure 2c) was generated with Mathematica using the level-set equations.[2]

Mouse procedures and tissue processing

All mouse experiments were performed according to European guidelines for the care and use of laboratory animals. Protocols were approved by the Committee on the Ethics of Animal Experiments of the Regierung von Oberbayern.

Animals were housed according to institutional regulations with *ad libitum* access to food and water. All mice were C57BL/6J background. For the endotoxemia model, female mice (16 weeks old) were challenged with 10 mg/kg LPS from *E. coli* (O111:B4) and treated with one single dose of 250 µg of apoMP$_1$ intraperitoneally or saline as control. 24 hours later, mice were euthanized by ketamine/xylacine overdose, retroorbital blood was collected, and the mice were flushed with 20 mL of ice-cold PBS-EDTA (5 mM EDTA). Lung, liver, kidney, and heart were isolated and embedded in Tissue Tek O.C.T. compound (Sakura Finetek) for analysis.

Immunofluorescence

Cryosections (4 µm) were fixed with cold acetone followed by antigen blockade using 5% goat serum/phosphate buffered saline. Next, sections were incubated overnight at 4 °C with the following primary antibodies: rat anti-mouse Ly6G (BD, 1:200), rabbit anti-mouse histone H4 (Abcam, 1:200), rabbit anti-mouse histone H4 Alexa 488 conjugated (Abcam, 1:200), rabbit anti-mouse citrullinated histone H3 (Abcam, 1:200), rat anti-mouse CD31-Alexa 455 conjugated (BioLegend, 1:50), goat anti-mouse myeloperoxidase (MPO, Millipore, 1:200). After extensive washing, sections were incubated with secondary antibodies conjugated with DyLight 477, Dylight 550, Alexa594, or DyLight 650 (Thermo Fisher, 1:500). Counterstain to visualize nuclei was performed by incubating with DAPI (Molecular Probes). Cell death (TUNEL$^+$ cells) was detected using ApopTag® Red *in situ* Apoptosis Detection Kit (Millipore) following the manufacturer's instructions. Immunofluorescence sections were imaged using a Leica TCS SP8 (Leica Microsystems) equipped with a UV laser, a freely tunable pulsed white light laser, hybrid detectors, and a 63X1.40 oil objective. Raw pictures were deconvolved with Huygens Professional (v.16.10, Scientific Volume Imaging) and maximum intensity projections of deconvolved data were generated with the Leica Application Suite X (v.3.1, Leica Microsystems). Histological sections were quantified by computer-assisted morphometric analysis using ImageJ software (National Institutes of Health).

Cell culture and activation

Mouse vascular aorta/smooth muscle cells (MOVAS) (ATCC, CRL-2797™) were cultured in complete medium (DMEM, Gibco) supplemented with 10 % fetal bovine serum (Gibco), 0.2 mg/mL G418 (Invitrogen), and 5 mM sodium pyruvate (Sigma). All cells were maintained in an incubator at 37 °C, 5 % CO_2. J774A.1 macrophages and SVEC4-10 endothelial cells (both ATCC) were cultured in complete medium (DMEM, Gibco) supplemented with 10 % fetal bovine serum (Gibco). HepG2 human hepatocytes were cultured in complete medium (EMEM, Gibco) supplemented with 10 % fetal bovine serum (Gibco).

Cell viability assays

Cells were incubated with 50 μg/mL histone H4 (Biomol) and indicated amounts of apoMP1. Cell viability was measured based on propidium iodide (PI) uptake. PI^+ cells were visualized using a climate chamber fluorescence microscope (Leica, DMi8) and quantified by ImageJ software.

Statistics

Statistical analysis was performed by GraphPad Prism 7 (GraphPad Software). The ROUT outlier function was used to exclude statistical outliers (Q = 1%). Normal distribution of the data was assessed using the D'Agostino-Pearson omnibus test for normality. Normally distributed data was tested by two-tailed unpaired *t*-test (one variable) or one-way ANOVA with Tukey's or Dunnet's correction (>2 variables). When two factors were analyzed, data was analyzed using two-way ANOVA with Tukey's correction. In all tests a 95% confidence interval was used, with which $p<0.05$ was considered a significant difference. Correlograms were generated using R. All data is represented as mean ± SEM.

Modeling peptide–lipid interactions for pore formers and pore inhibitors

The central hypothesis in this work is that there are peptides that can induce membrane curvatures to form pores in the membrane (ex: H4n induction of NGC ($\boldsymbol{K}$<0)), as well as peptides that can induce the "opposite" curvature, thereby potentially canceling the membrane remodeling activity of the former and inhibit pore formation (ex: apoMP$_1$ induction of PGC ($\boldsymbol{K}$>0)). We develop a theoretical model based on linear membrane elasticity to connect the structural tendency identified by SAXS to pore formation in membranes when combinations of both peptide types are present.

Single peptide interacting with a membrane

Our approach closely follows previous modeling of anisotropic, curvature-inducing proteins or peptides.[3-5] We assume the peptides couple to the local curvature of an isolated 2D membrane. Since NGC is inherently anisotropic, a single peptide induces not just a spontaneous mean curvature in the membrane, but also a spontaneous curvature tensor $h_{ij}^{\pm}(\theta)$, whose eigenvectors and eigenvalues give the directions and magnitudes of the largest and smallest membrane curvature induced by the peptide. The sign of the superscript denotes whether the peptide induces PGC or NGC, with

$$h_{ij}^{\pm}(\theta)=\begin{pmatrix}\cos\theta & -\sin\theta\\ \sin\theta & \cos\theta\end{pmatrix}\begin{pmatrix}\xi_1^{\pm} & 0\\ 0 & \xi_2^{\pm}\end{pmatrix}\begin{pmatrix}\cos\theta & \sin\theta\\ -\sin\theta & \cos\theta\end{pmatrix}, \qquad (1)$$

where $\xi_1^{\pm}$ and $\xi_2^{\pm}$ are the peptide-generated curvatures along the principal axes, and the angle θ describes the local orientation of the peptide with respect to a set of surface coordinates (x_1, x_2). For PGC, we assume $\xi_1^{+}=\xi_2^{+}$, whereas NGC has $\xi_1^{-}>0$ but $\xi_2^{-}<0$. We also define the vector function $\mathbf{X}(x_1, x_2)$ to describe the shape of the membrane neutral surface, a unit vector $\mathbf{N}(x_1, x_2)$ for the normal to the surface, and a local membrane curvature tensor $h_{ij}=\mathbf{N}\cdot\partial_i\partial_j\mathbf{X}$, where ∂_i denotes a partial derivative along the x_i direction. The mean curvature of the membrane is the trace of $h_{ij}(x_1, x_2)$ while the Gaussian curvature is its determinant. Since we expect the interaction energy to be

minimized when the membrane curvature matches the spontaneous curvature induced by the peptide, we consider an interaction of the form

$$E_{\pm}(\theta;x_1,x_2) = (k/2)[h_{ij}(x_1,x_2) - h_{ij}^{\pm}(\theta)]^2. \quad (2)$$

We assume the coupling k is the same for both peptide classes. Denoting the monolayer thickness as t, we define a dimensionless coupling constant $\lambda = k/(k_B T t^2)$ at temperature T (Boltzmann constant k_B) and rescale all curvatures by $1/t$. Being proportional to the interaction energy between a peptide and a flat membrane, $\lambda k_B T$ therefore provides a measure of how strongly the peptide couples to the membrane shape. Let c_1 and c_2 denote the maximum and minimum principal curvatures of the membrane respectively, measured in units of t, at (x_1, x_2). Expanding the tensor notation, the energy of a single peptide interacting with the membrane through Eq. (1) becomes[3-5]

$$E_{\pm}(\theta;c_1,c_2)/k_B T = \frac{\lambda}{2}\left(\left[(c_1-\xi_1^{\pm})^2+(c_2-\xi_2^{\pm})^2\right]\cos^2\theta+\left[(c_2-\xi_1^{\pm})^2+(c_1-\xi_2^{\pm})^2\right]\sin^2\theta\right). \quad (3)$$

This energy explicitly depends on the coordinates since the principal curvatures c_i are functions of the coordinates themselves. When $\theta = 0$, the peptide's maximal curvature is aligned with the membrane's and only the first term persists. On the other hand, if $\theta = \pi/2$, the peptide is rotated by ninety degrees and the peptide's maximal curvature is further penalized by being aligned with the membrane's smallest curvature (Figure S3a,b). The tensor notation accounts for intermediate-case angles in a concise format. Finally,

$$E_{\pm}^{F}/(k_B T) = E_{\pm}(\theta;0,0)/(k_B T) = \frac{\lambda}{2}\left[\xi_{1,\pm}^2+\xi_{2,\pm}^2\right] \quad (4)$$

represents the energy of a peptide in a locally flat region of the membrane, and is independent of both angle and coordinates.

Multiple peptide types (NGC-inducing and PGC-inducing) interacting with a membrane

We assume that bound peptide complexes can effectively function as a single unified peptide, and that such complexes do not strongly interact with one another, except by excluding other peptides

from binding to the membrane in their immediate vicinity. To account for a large number of peptides, we must statistically average over the location and orientation of each peptide. For reversible peptide–membrane binding, we assume peptides in solution are in equilibrium with bound peptides, so each species is characterized by a chemical potential $k_{\mathrm{B}}T\ln(n_{\pm})$, where $n_{\pm}$ is the volume fraction of each peptide species in solution, and a membrane binding energy $e_{\pm}^{B}$. We define $\mu_{\pm} = e_{\pm}^{B} + k_{\mathrm{B}}T\ln(n_{\pm})$ to account for both. We also assume different species subtend characteristic areas that are roughly identical — a reasonable approximation given the two prototypical peptides being compared are relatively similar in mass and peptide structure. To account for the excluded area of peptides on the membrane, we decompose the membrane area into sites of area A_0, which can either be occupied or unoccupied with only one peptide type. The Grand partition function for the peptides is found by summing (or integrating) over all possible peptide orientations, positions, and numbers binding to the membrane. This yields

$$\begin{aligned} Q &= \prod_{\text{sites}}\left(\int\frac{d\theta}{2\pi}e^{\beta\mu_{+}-\beta E_{+}(\theta;c_1,c_2)}+\int\frac{d\theta}{2\pi}e^{\beta\mu_{-}-\beta E_{-}(\theta;c_1,c_2)}\right) \\ &= \exp\left[\int\frac{dA}{A_0}\ln\left(1+\int\frac{d\theta}{2\pi}e^{\beta\mu_{+}-\beta E_{+}(\theta;c_1,c_2)}+\int\frac{d\theta}{2\pi}e^{\beta\mu_{-}-\beta E_{-}(\theta;c_1,c_2)}\right)\right], \end{aligned} \tag{5}$$

where $\beta=1/k_{\mathrm{B}}T$ and we have taken the continuum limit in the product over the membrane area in the last equality, and $\int dA$ denotes the integral over the membrane neutral surface. The *correction* to the Helfrich membrane energy is given by $\Delta F=-k_{\mathrm{B}}T\ln Q$, so that

$$\frac{\Delta F}{k_{\mathrm{B}}T} = -\frac{1}{A_0}\int dA\ln\left(1+\int\frac{d\theta}{2\pi}e^{\beta\mu_{+}-\beta E_{+}(\theta;c_1,c_2)}+\int\frac{d\theta}{2\pi}e^{\beta\mu_{-}-\beta E_{-}(\theta;c_1,c_2)}\right). \tag{6}$$

The two integrals over angles compute the statistical average over the orientations of the peptides at each site on the membrane, weighted by the energy. The integrand acquires position dependence from the variation of the membrane principal curvatures c_{i} from point to point.

To separate the contribution of the peptides to the membrane surface tension, we add and subtract the change in free energy for a peptide on a flat surface to obtain

$$\frac{\Delta F}{k_{\mathrm{B}}T} = -\frac{A}{A_0}\ln\left(1+e^{\beta\mu_+-\beta E_+^F}+e^{\beta\mu_--\beta E_-^F}\right)$$
$$-\frac{1}{A_0}\int dA\left[\ln\left(1+\int\frac{d\theta}{2\pi}e^{\beta\mu_+-\beta E_+(\theta;c_1,c_2)}+\int\frac{d\theta}{2\pi}e^{\beta\mu_--\beta E_-(\theta;c_1,c_2)}\right)-\ln\left(1+e^{\beta\mu_+-\beta E_+^F}+e^{\beta\mu_--\beta E_-^F}\right)\right] \quad (7)$$

The second term explicitly vanishes on a flat membrane, so a Taylor expansion in powers of membrane curvature will have no zeroth order term. It gives the entire correction to the Helfrich bending energy of a membrane, accounting for the energetics of interaction between peptide and membrane as well as the orientational and translational entropy of the peptides. The first term of Eq. (7) is proportional to area but not curvature, and captures the entire peptide contribution to the membrane surface tension. For a membrane in equilibrium with a lipid reservoir, it accounts for the change in membrane area due to the peptide binding. For example, if binding is highly favorable, the surface tension will decrease and the membrane area will correspondingly increase.

The second term can be better understood by expanding Eq. (7) in powers of membrane curvature. Schematically, this yields $\Delta F / k_{\mathrm{B}}T = -A\Delta\sigma + c_0(c_1+c_2) + \Delta\kappa(c_1+c_2)^2/2 + \Delta\bar{\kappa}c_1c_2 + \ldots$, where the correction to the surface tension from the first term is denoted $\Delta\sigma$, and expressions for the spontaneous curvature c_0 and bending moduli corrections, $\Delta\kappa$ and $\Delta\bar{\kappa}$, can be obtained but are very cumbersome. To summarize, the peptides act to change the effective bending moduli of the Helfrich model as well as induce a spontaneous curvature.

The integrals over θ can be obtained explicitly, yielding

$$\frac{\Delta F}{k_{\mathrm{B}}T} = -\frac{A}{A_0}\ln\left[1+\sum_{\pm}z_{\pm}\right]$$
$$-\int\frac{dA}{A_0}\ln\left\{1+\sum_{\pm}z_{\pm}\exp\left[-\frac{\lambda}{2}\left(c_1^2+c_2^2-(c_1+c_2)(\xi_{1,\pm}+\xi_{2,\pm})\right)\right]I_0\left[\frac{\lambda}{2}(c_1-c_2)(\xi_{1,\pm}-\xi_{2,\pm})\right]\right. \quad (8)$$
$$\left.-\ln\left[1+\sum_{\pm}z_{\pm}\right]\right\},$$

where $I_0(x) \geq 1$ is a modified Bessel function and is defined to be symmetric about $x = 0$, and $z_{\pm} = \exp\left[\mu_{\pm}/(k_{\mathrm{B}}T) - \lambda(\xi_{1,\pm}^2+\xi_{2,\pm}^2)/2\right]$ is a generalized fugacity for the peptides.

Finally, we note the expressions obtained for the peptide area fraction of either type:

$$\rho_{\pm} = \mathcal{N}^{-1} z_{\pm} \exp\left[-\frac{\lambda}{2}\left(c_1^2 + c_2^2 - (c_1 + c_2)(\xi_{1,\pm} + \xi_{2,\pm}) \right) \right] I_0 \left[\frac{\lambda}{2}(c_1 - c_2)(\xi_{1,\pm} - \xi_{2,\pm}) \right], \qquad (9)$$

where the normalization $\mathcal{N}$ is given by

$$\mathcal{N} = 1 + \sum_{\pm} z_{\pm} \exp\left[-\frac{\lambda}{2}\left(c_1^2 + c_2^2 - (c_1 + c_2)(\xi_{1,\pm} + \xi_{2,\pm}) \right) \right] I_0 \left[\frac{\lambda}{2}(\xi_{1,\pm} - \xi_{2,\pm}) \right]. \qquad (10)$$

The quantities $z_{\pm}$ can be interpreted by considering the area fraction on a flat membrane, for which $\rho_{\pm}^{F} = z_{\pm} / (1 + z_{+} + z_{-})$. Thus, the generalized fugacities are related to the average density of peptides on the flat regions of the membrane. Similarly, we can interpret the quantity λ by considering the additional cost of inserting a peptide on a flat membrane region rather than one for which the induced curvature is precisely matched by the membrane (see Eq. (4)).

Modeling of membrane pores

We describe a pore with the fixed shape of the inside of a torus (Figure S4), having $\mathbf{X} = [r + \cos\psi][\cos\phi\, \hat{x} + \sin\phi\, \hat{y}] + \sin\psi\, \hat{z}$, measured in units of t, for $\pi/2 \le \psi \le 3\pi/2$, $0 \le \phi \le 2\pi$ and pore radius $r \ge 1$. This yields principal curvatures c_1=1 and $c_2 = \cos\psi / [r + \cos\psi]$. The area measure is given by $dA = [r + \cos\psi]\, d\psi\, d\phi$. In the absence of peptides, pore formation is typically described using a model reminiscent of classical nucleation theory,[6, 7] with $F_{\text{bare}}/(k_B T) = -\sigma\pi r^2 + 2\pi r\Gamma$ for a circular pore of radius r with line tension Γ and a membrane surface tension σ. This free energy describes a barrier height $F_{\text{barrier}} = \pi\, k_B T\, \Gamma^2/\sigma$. As we saw earlier from Eq. (7), the presence of peptides modifies the bare line and surface tensions.

For given peptide fugacities and pore radii, we compute the free energy over the inner rim of a pore numerically using Eq. (8). We assume a bare line tension Γ of around 10^{-11} J/m, so using $t \approx$ 2 nm gives $\Gamma t \approx 5$. Similarly, a typical surface tension is 10^{-3} N/m^2, which gives $\sigma t^2 \approx 1$. We further assume $A_0 \approx t^2$ and $\lambda = 7.5$ which corresponds to an energy difference of ~4 $k_B T$ between a peptide bound to a flat membrane and one bound at a point at which the membrane exactly matches the

prescribed curvature of the peptide. Finally, we choose prescribed curvatures for the peptides by using the characteristic length scale of the bicontinuous cubic phases determined by X-ray scattering (Figure 2d). For $\boldsymbol{K}$<0-inducing (–) peptides, we set $\xi_{1,-} = 1/t \approx 0.5$ nm^{-1} commensurate with the curvature on the inside of a pore and $(\lambda/2)(\xi_1^2 + \xi_2^2) \approx 4k_{\mathrm{B}}T$ to give an average induced Gaussian membrane curvature of $\langle K \rangle \approx (0.3/t)^2\,\mathrm{nm}^{-2}$, consistent with a Schwarz' D (*Pn3m*) surface of lattice size 17 nm.[8, 9] A $\boldsymbol{K}$>0-inducing (+) peptide may induce different amounts of positive curvature stress along its two principal directions, but we adopt a simple model of isotropic curvature presentation by using $\xi_{1,+} = \xi_{2,+} = 0.3/t$ nm^{-1}. Figure 4a plots the energy barrier for opening a membrane pore in a mixture of $\boldsymbol{K}$>0-inducing (+) peptides (orange) and $\boldsymbol{K}$<0-inducing (–) peptides (green). Even at very modest area fractions, a $\boldsymbol{K}$>0-inducing (+) peptide will inhibit pore formation by raising the energy barrier drastically. We find that $\boldsymbol{K}$<0-inducing (–) peptides, like H4n, suppress the free energy barrier while $\boldsymbol{K}$>0-inducing (+) peptides, like apoMP$_1$, elevate it. Conversely, equilibrium *Pn3m* lattice constants a_{Pn3m} can be estimated by minimizing the free energy for given peptide-prescribed $\xi_{1,2}$ and H4n/apoMP$_1$ stoichiometry. We minimized *the sum* of the corrections from Eq. (8) and the Helfrich energy density

$$\frac{\varepsilon}{k_{\mathrm{B}}T} = \frac{\kappa}{2}(c_1 + c_2)^2 + \bar{\kappa} c_1 c_2, \qquad (11)$$

using literature values for the moduli $\bar{\kappa} = -0.83\,\kappa$ and $\kappa/(k_{\mathrm{B}}T)$=10.[10] See Figure 4b for computed a_{Pn3m} *versus* peptide stoichiometry. For the $\boldsymbol{K}$<0-inducing (–) peptide, peptide-prescribed curvatures were kept at $(\xi_1, \xi_2) = (1, -0.09)$, in units of 1/*t*, for maximum compatibility with a 17 nm *Pn3m* phase. For the $\boldsymbol{K}$>0-inducing (+) peptide, we varied curvatures isotropically ($\xi_1 = \xi_2$) from 0.3 to 0.74, in units of 1/*t*. Consistent with experimental trends, calculated *Pn3m* lattice constants generally grow with increasing molar ratio of $\boldsymbol{K}$>0-generating (apoMP$_1$) to $\boldsymbol{K}$<0-generating (H4n) peptides.

It is interesting to note that experimentally, upon addition of PGC-generating molecules to cubic phases induced by NGC-generating molecules, we see first a small initial decrease in the cubic lattice constant, followed by a sustained increase in the cubic lattice constant, followed finally by

a complete suppression of the cubic phase. (In other PGC/NGC systems, we have also seen the lattice constant of the cubic phase increase monotonically until the cubic phase is completely suppressed.) We rationalize this interesting behavior in the following manner. By definition, a cubic phase is characterized by zero mean curvature, which requires the quantitative amount of positive curvature to be the same as that of negative curvature in the system. However, for an arbitrary membrane-remodeling molecule that induces NGC, the amount of induced positive curvature is in general not necessarily the same as the amount of induced negative curvature. For example, if a molecule induces more negative curvature than positive curvature, a cubic phase can in principle still form at a different lattice constant at the expense of additional membrane stress. If one adds more PGC-inducing molecules to this system, it may allow the system to form optimal cubic phases with balanced positive and negative curvatures and thereby initially decrease the lattice constant from the stressed value, before so much PGC is added that the cubic phase itself is destabilized.

Supplemental Tables

Table S1. The symmetries, lattice parameters, and NGC values of cubic phases induced by histone H4n (PS/PE/CH 20/70/10), HIV-TAT (PS/PE 20/80), and protegrin-1 (PS/PE 20/80) in the absence and presence of apoMP$_1$.

ApoMP$_1$ P/L molar ratio	Histone H4n (P/L molar ratio = 1/40)	HIV-TAT (P/L molar ratio = 1/40)
0	Pn3m (a = 18.3 nm) $\langle K \rangle$ = –1.96 E–2 nm^{-2}	Pn3m (a = 19.6 nm) $\langle K \rangle$ = –1.70 E–2 nm^{-2}
1/100	Pn3m (a = 18.2 nm) $\langle K \rangle$ = –1.98 E–2 nm^{-2}	Pn3m (a = 17.0 nm) $\langle K \rangle$ = –2.26 E–2 nm^{-2}
1/50	Pn3m (a = 17.2 nm) $\langle K \rangle$ = –2.22 E–2 nm^{-2}	Pn3m (a = 15.3 nm) $\langle K \rangle$ = –2.79 E–2 nm^{-2}
1/25		

ApoMP$_1$ P/L molar ratio	Protegrin-1 (P/L molar ratio = 1/40)
0	Im3m (a = 18.0 nm) $\langle K \rangle$ = –3.3 E–2 nm^{-2} Pn3m (a = 14.5 nm) $\langle K \rangle$ = –3.13 E–2 nm^{-2}
1/120	Pn3m (a = 18.4 nm) $\langle K \rangle$ = –1.94 E–2 nm^{-2}
1/60	
1/30	

*Empty cells indicate the absence of cubic phases.

Table S2. The symmetries, lattice parameters, and NGC values of cubic phases induced by histone H4n (PS/PE/CH 20/70/10), melittin (PS/PE 20/80), and HIV-TAT (PS/PE 20/80) in the absence and presence of APP-2498.

APP-2498 P/L molar ratio	Histone H4n (P/L molar ratio = 1/40)	Melittin (P/L molar ratio = 1/25)	HIV-TAT (P/L molar ratio = 1/40)
0	Pn3m (a = 18.3 nm) $\langle K \rangle$ = –1.96 E–2 nm^{-2}	Im3m (a = 24.0 nm) $\langle K \rangle$ = –1.86 E–2 nm^{-2}	Pn3m (a = 19.6 nm) $\langle K \rangle$ = –1.70 E–2 nm^{-2}
1/100	Pn3m (a = 17.6 nm) $\langle K \rangle$ = –2.11 E–2 nm^{-2}	Im3m (a = 17.5 nm) $\langle K \rangle$ = –3.48 E–2 nm^{-2}	Pn3m (a = 20.0 nm) $\langle K \rangle$ = –1.64 E–2 nm^{-2}
1/50	Pn3m (a = 16.5 nm) $\langle K \rangle$ = –2.39 E–2 nm^{-2}		Pn3m (a = 18.0 nm) $\langle K \rangle$ = –2.02 E–2 nm^{-2}
1/25			

*Empty cells indicate the absence of cubic phases.

Supplemental Figures

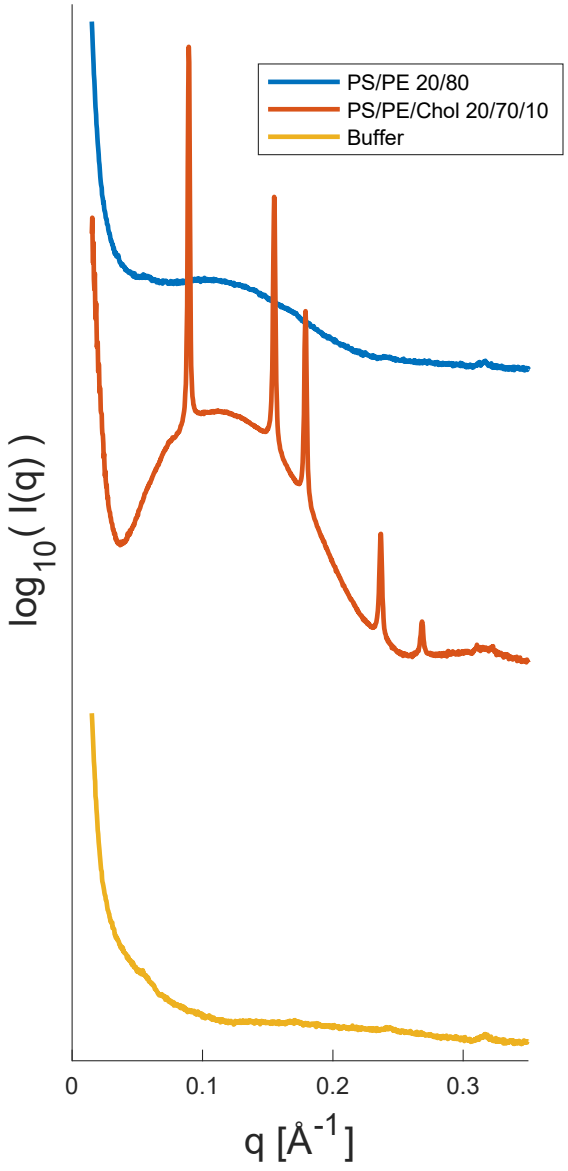

Figure S1. SAXS spectra for SUVs and buffer control samples. The SAXS profile of PS/PE 20/80 SUVs shows a form factor that is consistent with unilamellar vesicles and the SAXS spectrum of PS/PE/CH 20/70/10 SUVs indicates the existence of an H_{II} phase. Scattering from the buffer control sample shows background signal.

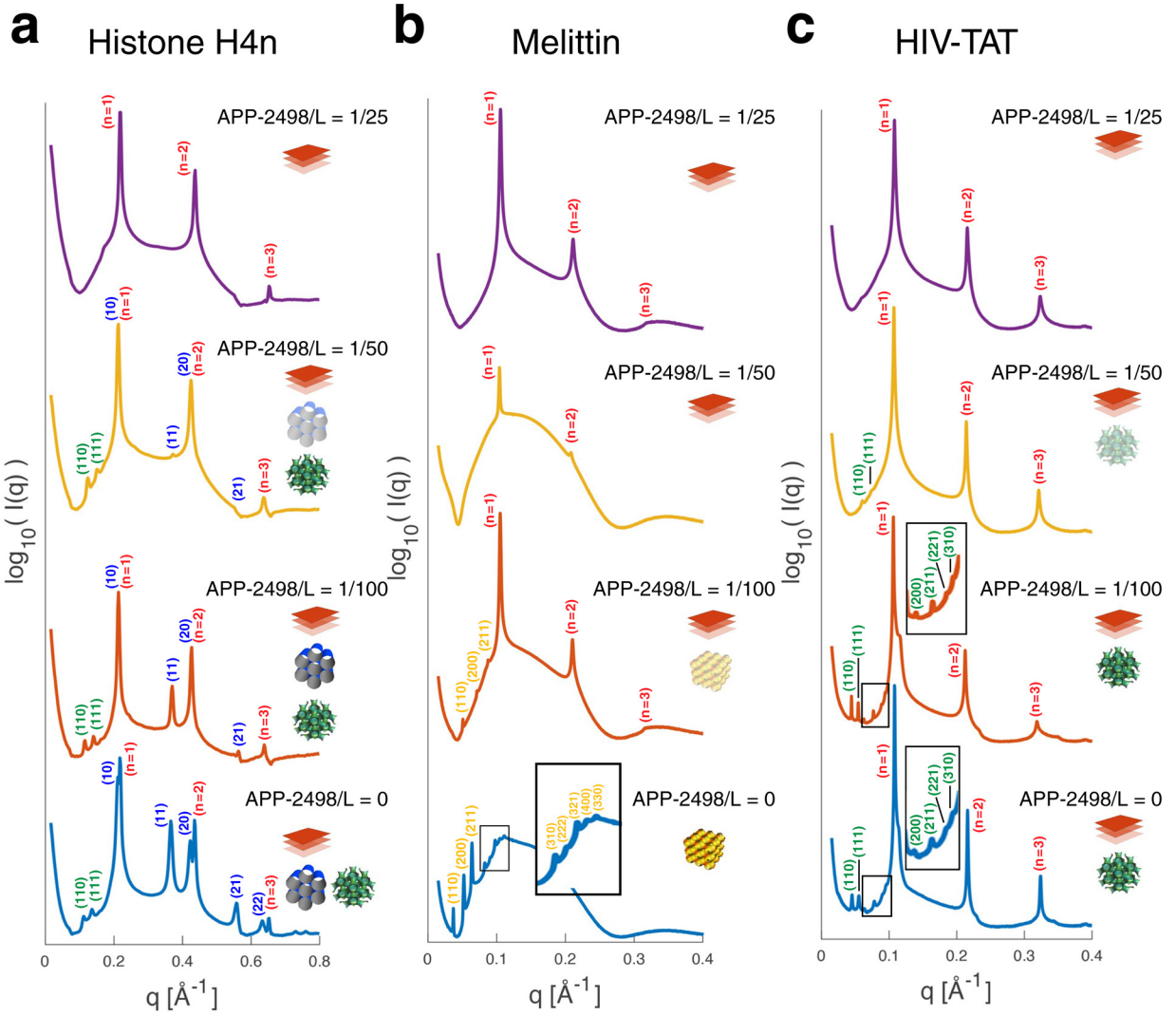

Figure S2. Anti-pore peptide APP-2498 inhibits the pro-lytic membrane activity of histone H4 N-terminus and unrelated peptides. (a) SAXS spectra of PS/PE/CH 20/70/10 SUVs incubated with H4n and APP-2498. The P/L molar ratio of H4n was held constant at 1/40, while the P/L molar ratio of APP-2498 was varied. H4n alone induced L_α, H_{II}, and *Pn3m* Q_{II} phases. *Pn3m* Q_{II} phases were suppressed at high concentrations of APP-2498. **(b)** SAXS spectra of PS/PE 20/80 SUVs co-treated with the AMP melittin[11] (NGC-generating peptide) and APP-2498. The P/L molar ratio of melittin was held constant at 1/25, while the P/L molar ratio of APP-2498 was varied. Melittin alone induced *Im3m* Q_{II} phases. *Im3m* Q_{II} phases were suppressed at high P/L molar ratios of APP-2498, while a zero-curvature L_α phase gradually emerged. **(c)** SAXS spectra of PS/PE 20/80 SUVs co-treated with the CPP HIV-TAT (NGC-generating peptide) and APP-2498. The P/L molar ratio of HIV-TAT was held constant at 1/40, while the P/L molar ratio of APP-2498 was varied. HIV-TAT alone induced L_α and *Pn3m* Q_{II} phases. *Pn3m* Q_{II} phases were suppressed at high P/L molar ratios of APP-2498, leaving behind only L_α phases with no curvature. **(a–c)** Observed reflections for the *Pn3m* cubic (green), *Im3m* cubic (yellow), hexagonal (blue), and lamellar (red) phases have been assigned on the curves.

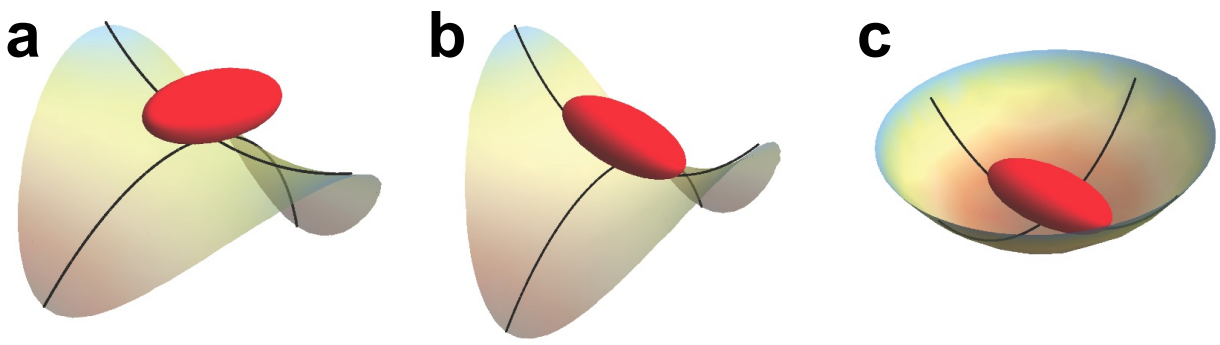

Figure S3. Peptide–membrane interaction. (a, b) The interaction between a membrane with NGC and an anisotropic peptide depends on the relative angle between the membrane principal curvatures (black lines) and the peptide orientation. This difference is captured by Eq. (2). **(c)** On the other hand, an anisotropic peptide on a locally isotropic membrane, such as a sphere, can rotate without changing the energy cost. This additional rotational entropy competes with the energy cost of mismatched peptide and membrane curvature.

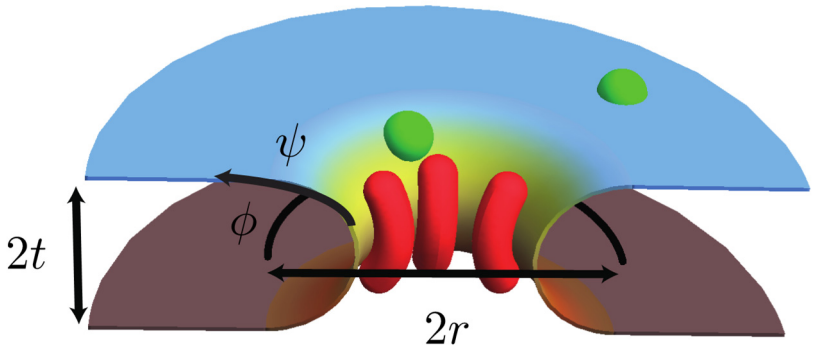

Figure S4. Schematic of a model membrane pore. Peptides with NGC (represented by red, bent cylinders) favor pore formation by better matching the NGC of the inner rim of the pore while peptides with PGC (green spheres) do not. These two curvature types compete to raise or lower the free energy barrier for pore formation. The pore is modeled by the inner surface of a torus of large radius r and small radius t, where t is the monolayer thickness.

Supplemental References

1. Ilavsky, J. Nika: Software for Two-Dimensional Data Reduction. *J. Appl. Crystallogr.* **2012**, *45*, 324–328.
2. Wohlgemuth, M.; Yufa, N.; Hoffman, J.; Thomas, E. L. Triply Periodic Bicontinuous Cubic Microdomain Morphologies by Symmetries. *Macromolecules* **2001**, *34*, 6083–6089.
3. Fournier, J. B. Nontopological Saddle-Splay and Curvature Instabilities from Anisotropic Membrane Inclusions. *Phys. Rev. Lett.* **1996**, *76*, 4436–4439.
4. Kralj-Iglič, V.; Heinrich, V.; Svetina, S.; Žekš, B. Free Energy of Closed Membrane with Anisotropic Inclusions. *Eur. Phys. J. B* **1999**, *10*, 5–8.
5. Fošnarič, M.; Kralj-Iglič, V.; Bohinc, K.; Iglič, A.; May, S. Stabilization of Pores in Lipid Bilayers by Anisotropic Inclusions. *J. Phys. Chem. B* **2003**, *107*, 12519–12526.
6. Litster, J. D. Stability of Lipid Bilayers and Red Blood Cell Membranes. *Phys. Lett. A* **1975**, *53*, 193–194.
7. García-Sáez, A. J.; Chiantia, S.; Salgado, J.; Schwille, P. Pore Formation by a Bax-Derived Peptide: Effect on the Line Tension of the Membrane Probed by AFM. *Biophys. J.* **2007**, *93*, 103–112.
8. Shearman, G. C.; Ces, O.; Templer, R. H.; Seddon, J. M. Inverse Lyotropic Phases of Lipids and Membrane Curvature. *J. Phys.: Condens. Matter* **2006**, *18*, S1105–S1124.
9. Lord, E. A.; Mackay, A. L. Periodic Minimal Surfaces of Cubic Symmetry. *Curr. Sci.* **2003**, *85*, 346–362.
10. Siegel, D. P.; Kozlov, M. M. The Gaussian Curvature Elastic Modulus of N-Monomethylated Dioleoylphosphatidylethanolamine: Relevance to Membrane Fusion and Lipid Phase Behavior. *Biophys. J.* **2004**, *87*, 366–374.
11. Matsuzaki, K.; Yoneyama, S.; Miyajima, K. Pore Formation and Translocation of Melittin. *Biophys. J.* **1997**, *73*, 831–838.